



A biphasic visco-hyperelastic damage model for articular cartilage: application to micromechanical modelling of the osteoarthritis-induced degradation behaviour

Dongxu Liu¹ · Songyun Ma¹ · Marcus Stoffel¹ · Bernd Markert¹

Received: 25 April 2019 / Accepted: 22 November 2019 / Published online: 4 December 2019
© Springer-Verlag GmbH Germany, part of Springer Nature 2019

Abstract

Osteoarthritis-induced microstructural and compositional changes of articular cartilage affect its load-bearing capacity and the damage resistance. The aim of the present study is to analyse effects of the osteoarthritis-induced microstructural degradation on the damage behaviour of articular cartilages. A poro-visco-hyperelastic damage model is proposed within the theoretical framework of continuum mechanics to describe the deformation and damage behaviour of collagen fibrils and highly hydrated proteoglycan matrix in articular cartilages. An integral-type nonlocal algorithm is employed to overcome the mesh dependence of simulation results involving strain localization. 3D computational models for a normal cartilage and two osteoarthritic cartilages with different degeneration levels are developed to study the degradation of the damage resistance of articular cartilages. In addition, the present simulations take into account the alterations of collagen fibril networks as well as compositional changes of cartilage constituents at different osteoarthritic stages. The material parameters of the constitutive model are identified by comparing the computational results to unconfined compression tests. The simulation results of spherical indentation tests show that damage in the articular cartilage with high-stage osteoarthritis is much more significant than that in the normal cartilage under identical loadings. The proposed computational methods can be used for studying the relationship between the damage behaviour and the complex morphology of the collagen fibril networks in biomaterials.

Keywords Articular cartilage · Osteoarthritis · Damage behaviour · Porous media · Poro-visco-hyperelastic · Nonlocal modelling

1 Introduction

Articular cartilage (AC) is a biological soft tissue, covering the ends of bones in synovial joints. Intact AC contributes to the ultra-low friction and superior load-bearing capacity of joints. Previous studies have demonstrated that the extraordinary mechanobiological properties of AC mainly result from its sophisticated microstructure and compositions (Mäkelä et al. 2018). AC is primarily composed of collagen fibrils (type II) and highly hydrated proteoglycan (PG) matrix (Mäkelä et al. 2018; Inamdar et al. 2017). Collagen fibrils account for about two-thirds of the dry weight (He et al. 2013). Previous studies revealed that in the deep zone

(DZ) fibrils were perpendicular to the subchondral bone, while in the middle zone (MZ) fibrils gradually bended over and finally oriented in the direction parallel to the cartilage surface in the superficial zone (SZ) (Clark 1990, 1991; Wilson et al. 2006a). Primary collagen fibrils interact with each other by transversely oriented interconnections, namely cross-links, to build scaffold-like fibrillar networks (Nickien et al. 2013; Thambyah and Broom 2007). However, microstructural and compositional changes of AC can be induced by ageing or diseases, resulting in a deteriorated mechanical performance of AC. Additionally, abnormal loading conditions, such as repetitive impacts, over twisting and excessive loading, can lead to intense compression or shear stresses and thereby cause damage to AC. Due to the poor regeneration capacity, damaged AC is likely to develop into osteoarthritis (OA) (Stender et al. 2015).

OA is a degenerative joint disease, directly related to changes of microstructure and compositions of AC, i.e. PG depletion, collagen fibril network degradation and increased

✉ Songyun Ma
ma@iam.rwth-aachen.de

¹ Institute of General Mechanics, RWTH Aachen University, Aachen, Germany

fluid content (Arokoski et al. 2000). In the progression of OA, tension stiffness of fibrils continuously decreases and fibril networks are significantly disorganized (Saarakkala et al. 2010). In addition, cross-links between primary fibrils break, resulting in the disruption of collagen networks and thereby decreasing the overall tension stiffness of AC (Mansfield et al. 2015; Natarajan et al. 2015). Declined reinforcement effects of collagen fibril networks lead to less resistance to the lateral expansion of PG, increased permeability of AC and the degradation of overall load-bearing capacity (Mow et al. 1984; He et al. 2013). Moreover, since AC lacks blood vessels, nerves and lymphatic tissue, early OA is difficult to be diagnosed and self-repaired (Mow et al. 1992). OA has been a leading cause of chronic disability worldwide (Hui Mingalone et al. 2018). Therefore, a comprehensive insight into the interrelationship between the damage behaviour and OA-induced alterations of microstructure and composition is urgent for a better understanding of the pathogenesis of OA.

To date, experimental investigation is one of the main approaches to study the initiation and progression of OA, as well as the damage behaviour of AC (Stender et al. 2015; Hui Mingalone et al. 2018). In the past decades, mechanical experiments from the nanoscale to the macroscale have been conducted to study the effects of OA on the mechanical behaviours of AC (Julkunen et al. 2008; Doyran et al. 2017). However, the micromechanical properties of the microstructure in AC are difficult, if not impossible, to be experimentally identified due to the limitation of the current experimental technologies (Stender et al. 2015, 2016; Saarakkala et al. 2010; He et al. 2013). Moreover, the interactions between the OA-induced microstructural changes and the degraded damage resistance of osteoarthritic AC cannot be investigated by experiments. Computational simulation is regarded as a useful method to facilitate the understanding of the structure–property relationships of AC, in addition to experiments. Due to the complex mechanical behaviour of AC and pathologies of OA, accurate constitutive models are needed to precisely describe the mechanical response in computational simulations. Stender et al. (2015) proposed an anisotropic constitutive model to study the damage initiation and development of AC from a newborn bovine. In this work, the viscoelastic behaviour and the effect of fluid flows were not considered in the constitutive model, which can lead to an inaccurate prediction of the realistic damage response under dynamic loads. Hosseini et al. (2014) developed a fibril-reinforced viscoelastic biphasic model to predict the mechanically induced damage progression in AC based on the prior work of Wilson et al. (2006b). They attempted to analyse the interrelationship of the damage behaviour of fibrils and PG during the progression of AC damage. Párraga Quiroga et al. (2017) used computational simulations to analyse the effects of loading rates on the

damage response of AC. In their models, only the distribution of orientations of the primary and secondary collagen fibrils is taken into account. The interconnections (cross-links) between primary and secondary fibrils were neglected. However, the morphology of the collagen fibril network plays a crucial role in the deformation and damage resistance of AC (Gottardi et al. 2016; Klika et al. 2016; Inamdar et al. 2017; Nickien et al. 2013; Changor et al. 2011).

Despite that a large number of constitutive models have been proposed for AC, most of them focused mainly on the normal AC. Only very limited studies discussed the influence of OA progression on the deformation and damage behaviour of AC (Saarakkala et al. 2010; Vanden Berg-Foels et al. 2012; Gottardi et al. 2016). Korhonen et al. (2003) applied a poroelastic model to investigate the effect of OA-induced PG depletion and collagen degradation on the stress–relaxation response, in which they ignored the intrinsic viscoelasticity of solid constituents. Richard et al. (2013) proposed an isotropic viscoelastic model to predict the mechanical response of human normal and OA cartilages, where the effects of fluid flows were not involved. However, previous studies suggested that the coupling of both solid intrinsic viscoelasticity and flow-dependent viscoelasticity should be involved in the model to describe the rate-dependent mechanical response of AC (DiSilvestro and Suh 2001; García and Cortés 2007). In addition, both the above-mentioned two studies captured the OA-induced tissue degeneration only by reducing the material stiffness, while the microstructural alterations of collagen fibrils caused by OA were not taken into account in the computational simulations (Korhonen et al. 2003; Richard et al. 2013). In order to study the effect of OA-induced microstructural changes on the mechanical response of AC, Liukonen et al. (2017) and Mononen et al. (2016) proposed cartilage degeneration algorithms in their recent works. In these studies, collagen fibrillation was simulated by decreasing the collagen network stiffness, while the OA-induced softening and overloading-induced damage of PG matrix, as well as the compositional changes, were neglected. Due to the mechanical interactions between the PG matrix and collagen fibrils, the damage of PG matrix may have significant influence on the damage behaviour of collagen fibrils (Men et al. 2017; Hosseini et al. 2014), and these two mechanisms of tissue damage should be considered simultaneously in simulations. Therefore, a computational simulation involving the biphasic and solid viscoelastic effects, as well as the OA-induced microstructural and compositional changes, is needed to accurately investigate the effects of OA on the deformation and damage behaviours of AC.

In the present study, a biphasic visco-hyperelastic damage model is developed within the framework of finite strains to describe the nonlinear deformation behaviour and the damage progression of articular cartilages. The morphology of

the fibril network of AC is explicitly modelled in the computational simulations. In order to overcome the mesh dependence of numerical simulations involving strain localizations (Ma and Yuan 2015), an integral-type nonlocal averaging scheme (Ferreira et al. 2017; Ma et al. 2018) is coupled to the proposed damage model. The aim of this work is to investigate the effect of OA-induced microstructural changes of collagen fibril network on the damage behaviour of AC. Three-dimensional finite element models of osteoarthritic cartilages with different degrees of OA were built. A finite element model of an intact cartilage was also presented for comparison. The morphological microstructures of interconnections in collagen fibril networks were taken into account. Depth-based microstructural and compositional information was included into the finite element models. Model parameters were identified based on previous experimental and computational studies on cartilages. The demonstrated simulation results in articular cartilage show that the proposed computational methods can be used for studying the deformation and damage behaviour of biological tissues and biomaterials with a complex morphology of collagen fibril networks.

2 Modelling of the deformation and damage behaviour of articular cartilage at finite strains

Previous studies have shown that the PG matrix and collagen fibrils in AC have different load-bearing modes, e.g. collagen fibrils mainly resist tension, while the PG matrix supports most compressive loads (Hosseini et al. 2014; Han et al. 2011; Hollander et al. 1994; Wilson et al. 2005). In addition, the PG matrix is a hydrated porous material, while collagen is nearly a monophasic tissue. Thereby, different constitutive models should be proposed to describe the mechanical behaviour for these two compositions. In this section, constitutive models are proposed within the framework of finite strains for the PG matrix and collagen fibrils. In addition, the porous media theory is utilized to capture the interaction of the solid and fluid phases of the PG matrix, which is assumed to be a saturated biphasic material. The mechanical behaviours of the constituents are assumed as isotropic. However, the anisotropic deformation behaviour of AC is reflected by the zonal morphology of collagen fibril networks.

2.1 Mixture theory

In the mixture theory, a saturated biphasic continuum is composed of an intrinsically incompressible solid matrix and incompressible interstitial fluid. The postulation of the material incompressibility is feasible since the volumetric

compressibility of an individual constituent in AC is much smaller than the change of void space due to hydrostatic pressurization (Ricken et al. 2010). In addition, the experimental study by Bachrach et al. supported that the solid matrix of AC was intrinsically incompressible under the normal physiologic hydrostatic pressures (Bachrach et al. 1998). In this work, both constituents are assumed to be immiscible materials, which are constitutively interconnected by interaction quantities, i.e. mass exchange, energy exchange and interaction forces. Herein, the mass exchange and energy exchange are neglected.

We use $[\bullet]^{\alpha}$ to denote a non-kinematical quantity of the constituents φ^{α} , where $\alpha = \{S, F\}$ represent the solid skeleton and pore fluid, respectively. $[\bullet]_{\alpha}$ indicates a kinematic quantity of the constituent φ^{α} . $[\bullet]'_{\alpha}$ denotes the material time derivative following the motion of the constituent φ^{α} . In the current configuration, the volume element dv and the mass element dm for the whole mixture φ are, respectively, given as

$$dv = dv^S + dv^F, \quad dm = dm^S + dm^F, \quad (1)$$

where dv^{α} and dm^{α} denote the partial volume element and partial mass element of the constituents φ^{α} , respectively. The volume fractions of the solid and fluid in the current configuration are defined as

$$n^S = \frac{dv^S}{dv}, \quad n^F = \frac{dv^F}{dv}, \quad (2)$$

respectively. The saturation condition is expressed as

$$n^S + n^F = 1. \quad (3)$$

The realistic density of φ^S and φ^F is defined as

$$\rho^{SR} = \frac{dm^S}{dv^S}, \quad \rho^{FR} = \frac{dm^F}{dv^F}, \quad (4)$$

respectively. The partial density of φ^S and φ^F in the current configuration is defined as

$$\rho^S = \frac{dm^S}{dv} = n^S \rho^{SR}, \quad \rho^F = \frac{dm^F}{dv} = n^F \rho^{FR}, \quad (5)$$

respectively. Following this, the mixture density ρ of the mixture φ in the current configuration is introduced as the sum of partial densities ρ^{α} ,

$$\rho = \rho^S + \rho^F. \quad (6)$$

Since both constituents φ^{α} are assumed to be intrinsically incompressible, the realistic densities ρ^{SR} and ρ^{FR} are constants. Thereby, the material time derivative of $\rho^{\alpha R}$ is zero, i.e. $[\rho^{\alpha R}]'_{\alpha} = 0$. It is noted that although both constituents are assumed to be intrinsically incompressible, material volume expansion or contraction due to fluid influx or efflux from

the solid skeleton can lead to the change of the partial density and the mixture density.

2.1.1 Kinematics

For the description of kinematics of material points in the porous media theory, \mathbf{X}_α denotes the position vector of a material point of the constituent φ^α in the reference configuration. \mathbf{x} denotes the position vector of a material point in the current configuration. It is noted that at any time t each spatial point \mathbf{x} is simultaneously occupied by a fluid particle and a solid particle. The displacement vector of the solid phase describes the solid motion $\mathbf{u}_S = \mathbf{x} - \mathbf{X}_S$. The deformation gradient \mathbf{F}_α is defined as $\mathbf{F}_\alpha = \frac{\partial \mathbf{x}}{\partial \mathbf{X}_\alpha}$. The two material points of both constituents φ^α , occupying the same spatial point \mathbf{x} , proceed from different reference positions \mathbf{X}_α at time $t = t_0$. The Jacobian J_α of φ^α is defined as $J_\alpha = \det \mathbf{F}_\alpha$. The right Cauchy–Green deformation tensor is defined as $\mathbf{C}_\alpha = \mathbf{F}_\alpha^T \mathbf{F}_\alpha$.

2.1.2 Balance equations

Ignoring mass exchanges between both constituents, the local balance equations of mass for the individual constituents φ^α are given by

$$[\rho^\alpha]_\alpha' + \rho^\alpha \operatorname{div} \dot{\mathbf{x}}_\alpha = 0, \quad (7)$$

where $\operatorname{div} [\bullet]$ denotes the spatial divergence operator with respect to \mathbf{x} and $\dot{\mathbf{x}}_\alpha$ represents the velocity vectors of the constituent φ^α . By using of the relation $\rho^\alpha = n^\alpha \rho^{\alpha R}$ and the incompressible condition $[\rho^{\alpha R}]_\alpha' = 0$, Eq. (7) is reduced to the volume balance

$$[n^\alpha]_\alpha' + n^\alpha \operatorname{div} \dot{\mathbf{x}}_\alpha = 0. \quad (8)$$

The material time derivative of a scalar quantity depending on \mathbf{x} and t is defined as

$$[\bullet]'_\alpha = \frac{\partial [\bullet]}{\partial t} + \operatorname{grad} [\bullet] \cdot \dot{\mathbf{x}}_\alpha, \quad (9)$$

where $\operatorname{grad} [\bullet]$ is the gradient operator with respect to spatial position vector \mathbf{x} . Combining the saturation condition Eq. (3), volume balance Eqs. (8) and (9), the continuity equation for the mixture is derived as

$$\operatorname{div} \dot{\mathbf{x}}_S + \operatorname{div} \mathbf{w}_F = 0, \quad (10)$$

where the term $\mathbf{w}_F = n^F \mathbf{w}_{FR}$ is called fluid filter velocity, with the seepage velocity $\mathbf{w}_{FR} = \dot{\mathbf{x}}_F - \dot{\mathbf{x}}_S$. With the assumption that inertial effects are neglected, and combining the balance equation of mass in Eq. (8), the local balance equation of linear momentum for the constituent φ^α is derived as

$$\operatorname{div} \mathbf{T}^\alpha + \rho^\alpha \mathbf{b} + \hat{\mathbf{p}}^\alpha = \mathbf{0}, \quad (11)$$

where \mathbf{b} is the body force acting on the mixture. Herein, we assume that both constituents undergo the same external acceleration. Therefore, the body force \mathbf{b}^α acting on each constituent φ^α is equal to \mathbf{b} ($\mathbf{b} = \mathbf{b}^\alpha$). The quantity \mathbf{T}^α is the partial Cauchy stress in the constituent φ^α . The total Cauchy stress \mathbf{T} in the mixture is the sum of the partial stress \mathbf{T}^S in φ^S and the partial stress \mathbf{T}^F in φ^F , which is written in the form

$$\mathbf{T} = \mathbf{T}^S + \mathbf{T}^F. \quad (12)$$

The quantity $\hat{\mathbf{p}}^\alpha = \hat{\mathbf{p}}^\alpha(\mathbf{x}, t)$ in Eq. (11) denotes the extra momentum production of the constituent φ^α . The extra momentum production terms are restricted by the relation

$$\hat{\mathbf{p}}^S = -\hat{\mathbf{p}}^F, \quad (13)$$

due to the overall conservation of momentum. According to the balance of moment of momentum for homogenized nonpolar materials, the partial Cauchy stress tensor of every constituent φ^α is symmetric, i.e.

$$\mathbf{T}^\alpha = [\mathbf{T}^\alpha]^T. \quad (14)$$

2.1.3 Constitutive equations

In order to derive the constitutive restrictions, we postulate the existence of a Helmholtz free energy ψ^α per unit mass of the constituent φ^α . The viscous properties of the interstitial fluid are neglected (Ricken et al. 2010). Accordingly, the Helmholtz free energy of the fluid constituent ψ^F is independent of any process variable, i.e.

$$\psi^F = \psi^F(-). \quad (15)$$

The Helmholtz free energy ψ^S of the solid constituent is postulated to explicitly depend on the right Cauchy–Green deformation tensor \mathbf{C}_S , the second-order tensorial internal variables $\boldsymbol{\Gamma}_\phi^S$ ($\phi = 1, 2, \dots, j$) and the isotropic damage variable d . The damage variable d represents the deterioration of the mechanical integrity of the solid skeleton due to microcracking. The free energy ψ^S is written in the form

$$\begin{aligned} \psi^S(\mathbf{C}_S, d, \boldsymbol{\Gamma}_1^S, \dots, \boldsymbol{\Gamma}_j^S) &= \psi_{\text{eq}}^S(d, \mathbf{C}_S) \\ &\quad + \psi_{\text{neq}}^S(\mathbf{C}_S, \boldsymbol{\Gamma}_1^S, \dots, \boldsymbol{\Gamma}_j^S) \\ &= [1 - d]\psi_{\text{eq}0}^S(\mathbf{C}_S) \\ &\quad + \psi_{\text{neq}}^S(\mathbf{C}_S, \boldsymbol{\Gamma}_1^S, \dots, \boldsymbol{\Gamma}_j^S). \end{aligned} \quad (16)$$

In Eq. (16), ψ_{eq}^S denotes the Helmholtz free energy for the thermodynamic equilibrium state, while ψ_{neq}^S is the corresponding Helmholtz free energy in the damage-free

configuration (without coupling to the damage variable). ψ_{neq}^S contributes to the viscoelastic response of material at thermodynamic non-equilibrium state, i.e. stress relaxation and/or creep behaviour (Holzapfel and Gasser 2001). Herein, Γ_ϕ^S ($\phi = 1, 2, \dots, j$) are like the right Cauchy–Green deformation tensor \mathbf{C}_S and characterize the viscoelastic response of the solid constituent. d is the damage variable which is derived in Sect. 2.2.

During the damage process of soft tissues, the irreversible energy dissipation obeys the second law of thermodynamics. Under the isothermal condition, the dissipation $\mathfrak{D}_{\text{int}}$ of the mixture is described by the Clausius–Duhem inequality

$$\begin{aligned} \mathfrak{D}_{\text{int}} &= \mathbf{T}^S \cdot \mathbf{D}_S + \mathbf{T}^F \cdot \mathbf{D}_F - \rho^S (\psi^S)'_S \\ &\quad - \rho^F (\psi^F)'_F - \hat{\mathbf{p}}^F \cdot \mathbf{w}_{FR} \geq 0, \end{aligned} \quad (17)$$

where \mathbf{D}_α is the deformation rate tensor of φ^α and is related to the spatial velocity gradient tensor by $\mathbf{L}_\alpha = \mathbf{D}_\alpha + \mathbf{W}_\alpha = \dot{\mathbf{F}}_\alpha \mathbf{F}_\alpha^{-1}$. Herein, \mathbf{W}_α is a skew-symmetric tensor. $[\bullet] \cdot [\bullet]$ represents the scalar product of two vectors or double contraction of two second-order tensors. Since the mixture is assumed to be fully saturated and the fluid and solid constituents are assumed to be intrinsically incompressible, the change of the volume fraction n^α in the process of deformation must fulfil the saturation constraint in Eq. (3). The saturation condition is guaranteed by adding the material time derivative of Eq. (3) weighted by a Lagrangian multiplier p to the entropy inequality Eq. (17),

$$\begin{aligned} \mathfrak{D}_{\text{int}} &= \mathbf{T}^S \cdot \mathbf{D}_S + \mathbf{T}^F \cdot \mathbf{D}_F - \rho^S (\psi^S)'_S - \rho^F (\psi^F)'_F \\ &\quad - \hat{\mathbf{p}}^F \cdot \mathbf{w}_{FR} - p [n^S + n^F]'_S \geq 0 \end{aligned} \quad (18)$$

By using the balance equations of mass Eq. (8) and Eq. (9), the material time derivative of the saturation equation Eq. (3) following the solid motion reads

$$[n^S + n^F]'_S = -[\mathbf{n}^S \mathbf{I} \cdot \mathbf{D}_S + \mathbf{n}^F \mathbf{I} \cdot \mathbf{D}_F + \text{grad } n^F \cdot \mathbf{w}_{FR}], \quad (19)$$

where the relation $\text{div } \dot{\mathbf{x}}_\alpha = \mathbf{D}_\alpha \cdot \mathbf{I}$ is used. The material time derivative of ψ^F and ψ^S in Eq. (18) is, respectively, calculated as

$(\psi^F)'_F = 0$, and

$$\begin{aligned} (\psi^S)'_S &= \mathbf{F}_S \left[2 \frac{\partial \psi^S}{\partial \mathbf{C}_S} + \sum_{\phi=1}^j 2 \frac{\partial \psi_{\text{neq}\phi}^S}{\partial \mathbf{C}_S} \right] \mathbf{F}_S^T \cdot \mathbf{D}_S \\ &\quad + \sum_{\phi=1}^j 2 \frac{\partial \psi_{\text{neq}\phi}^S}{\partial \Gamma_\phi^S} \cdot \frac{(\Gamma_\phi^S)'_S}{2} + \frac{\partial \psi_{\text{eq}}^S}{\partial d} \dot{d}, \end{aligned} \quad (20)$$

using the relation $\dot{\mathbf{C}}_S = 2\mathbf{F}_S^T \mathbf{D}_S \mathbf{F}_S$. Inserting Eqs. (20) and (19) into Eq. (18), the Clausius–Duhem inequality is rewritten as

$$\begin{aligned} \mathfrak{D}_{\text{int}} &= \left[\mathbf{T}^S + n^S p \mathbf{I} - \rho^S \mathbf{F}_S \left[2 \frac{\partial \psi_{\text{eq}}^S}{\partial \mathbf{C}_S} + \sum_{\phi=1}^j 2 \frac{\partial \psi_{\text{neq}\phi}^S}{\partial \mathbf{C}_S} \right] \mathbf{F}_S^T \right] \\ &\quad \cdot \mathbf{D}_S + [\mathbf{T}^F + n^F p \mathbf{I}] \cdot \mathbf{D}_F - \rho^S \sum_{\phi=1}^j 2 \frac{\partial \psi_{\text{neq}\phi}^S}{\partial \Gamma_\phi^S} \cdot \frac{(\Gamma_\phi^S)'_S}{2} \\ &\quad - \rho^S \frac{\partial \psi_{\text{eq}}^S}{\partial d} \dot{d} - [\hat{\mathbf{p}}^F - p \text{grad } n^F] \cdot \mathbf{w}_{FR} \geq 0. \end{aligned} \quad (21)$$

Since the strain rate \mathbf{D}_α in (21) can be chosen arbitrarily, in order to satisfy the admissible conditions, the partial Cauchy stress \mathbf{T}^α has to fulfil the thermodynamic restrictions

$$\begin{aligned} \mathbf{T}^S &= -n^S p \mathbf{I} + \mathbf{T}_E^S, \\ \mathbf{T}^F &= -n^F p \mathbf{I}, \end{aligned} \quad (22)$$

where p denotes the pore pressure, \mathbf{I} is the second-order identity tensor and \mathbf{T}_E^S is defined as the effective solid stress. Note that the viscous stress in the interstitial fluid is neglected and the Cauchy stress in the solid constituent \mathbf{T}^S is split into an effective solid pressure $-n^S p \mathbf{I}$ and an effective solid stress \mathbf{T}_E^S . Following Eqs. (21) and (22), the effective solid stress \mathbf{T}_E^S is written as

$$\mathbf{T}_E^S = \rho^S \mathbf{F}_S \left[2 \frac{\partial \psi_{\text{eq}}^S}{\partial \mathbf{C}_S} + \sum_{\phi=1}^j 2 \frac{\partial \psi_{\text{neq}\phi}^S}{\partial \mathbf{C}_S} \right] \mathbf{F}_S^T. \quad (23)$$

Following the structure in Eq. (16), the effective solid stress tensor \mathbf{T}_E^S is written as two separate terms: an equilibrium hyperelastic term $\mathbf{T}_{E,\text{eq}}^S$ and a time-dependent term $\mathbf{T}_{E,\text{neq}}^S$. Thus, the effective solid stress is written in the form

$$\mathbf{T}_E^S = \mathbf{T}_{E,\text{eq}}^S + \mathbf{T}_{E,\text{neq}}^S \quad (24)$$

The terms $\mathbf{T}_{E,\text{eq}}^S$ and $\mathbf{T}_{E,\text{neq}}^S$ are, respectively, defined as

$$\begin{aligned} \mathbf{T}_{E,\text{eq}}^S &= \rho^S \mathbf{F}_S 2 \frac{\partial \psi_{\text{eq}}^S}{\partial \mathbf{C}_S} \mathbf{F}_S^T, \\ \mathbf{T}_{E,\text{neq}}^S &= \rho^S \mathbf{F}_S \sum_{\phi=1}^j 2 \frac{\partial \psi_{\text{neq}\phi}^S}{\partial \Gamma_\phi^S} \mathbf{F}_S^T = J_S^{-1} \mathbf{F}_S \sum_{\phi=1}^j \mathbf{S}_{\text{neq}\phi}^S \mathbf{F}_S^T, \end{aligned} \quad (25)$$

where the internal variables $\mathbf{S}_{\text{neq}\phi}^S$ ($\phi = 1, 2, \dots, j$) are the stresses at the non-equilibrium thermodynamics state. $\mathbf{S}_{\text{neq}\phi}^S$ is conjugated to the tensorial internal variable Γ_ϕ^S . Following the work of Holzapfel and Gasser (2001), we restrict the viscoelastic free energy $\psi_{\text{neq}\phi}^S$ by the internal constitutive conditions $\mathbf{S}_{\text{neq}\phi}^S = -\rho_{0S}^S 2 \frac{\partial \psi_{\text{neq}\phi}^S}{\partial \Gamma_\phi^S}$ ($\phi = 1, 2, \dots, j$), where $\mathbf{S}_{\text{neq}\phi}^S$ is the ϕ -th time-dependent stress, $\rho_{0S}^S = n_{0S}^S \rho^{SR}$ is the partial solid density in the reference configuration and n_{0S}^S is the volume fraction of φ^S in the reference configuration. Thereby, the term in the internal dissipation in Eq. (21) reads

$$-\rho^S \sum_{\phi=1}^j 2 \frac{\partial \psi_{\text{neq}\phi}^S}{\partial \Gamma_\phi^S} \cdot \frac{(\Gamma_\phi^S)'_S}{2} = J_S^{-1} \sum_{\phi=1}^j \mathbf{S}_{\text{neq}\phi}^S \cdot \frac{(\Gamma_\phi^S)'_S}{2} \geq 0 \quad (\phi = 1, 2, \dots, j).$$

In order to derive the non-equilibrium stress $\mathbf{S}_{\text{neq}\phi}^S$, an evolution equation is specified to govern the evolution of this stress variable. Here, a generalized three-dimensional Zener model, containing one Hooke element and j paralleled Maxwell elements, is employed (Holzapfel and Gasser 2001; Kaliske and Rother 1997). Using this model, a set of linear differential equations are derived as

$$\dot{\mathbf{S}}_{\text{neq}\phi}^S + \frac{1}{\tau_\phi} \mathbf{S}_{\text{neq}\phi}^S = \gamma_\phi \dot{\mathbf{S}}_{\text{eq}0}^S, \quad (26)$$

where τ_ϕ is the relaxation time and γ_ϕ is a dimensionless free energy factor controlling the ratio between the spring stiffness in a Maxwell element and the Hooke element. $\mathbf{S}_{\text{eq}0}^S$ in Eq. (26) is the damage-free, second Piola–Kirchhoff stress $\mathbf{S}_{\text{eq}0}^S = \rho_0^S 2 \frac{\partial \psi_{\text{eq}0}^S}{\partial \mathbf{C}_S}$ in solid at the equilibrium state. The solution of this differential equation Eq. (26) is a convolution integral

$$\mathbf{S}_{\text{neq}\phi}^S = \int_0^t \gamma_\phi \exp \left[-\frac{t-s}{\tau_\phi} \right] \dot{\mathbf{S}}_{\text{eq}0}^S(s) ds. \quad (27)$$

τ_ϕ and γ_ϕ are user-specified parameters according to material properties. In the reference configuration, we assume a stress-free state, i.e., $\mathbf{S}_{\text{neq}\phi}^S|_{t=0} = \mathbf{0}$.

In order to satisfy the entropy inequality Eq. (18), the last term in Eq. (18) should be not less than zero, i.e.

$$-[\hat{\mathbf{p}}^F - p \operatorname{grad} n^F] \cdot \mathbf{w}_{FR} \geq 0. \quad (28)$$

A representation for $\hat{\mathbf{p}}^F$ is applied to fulfil this inequality Eq. (28) and is given in the form

$$\hat{\mathbf{p}}^F = p \operatorname{grad} n^F - \mathbf{H}^F \mathbf{w}_{FR}, \quad (29)$$

where \mathbf{H}^F represents a positive definite material parameter tensor. Substituting the terms \mathbf{T}^F and $\hat{\mathbf{p}}^F$ in the balance equation of the momentum for the fluid constituent in Eq. (11) with Eqs. (22) and (29), the balance equation of the momentum for the fluid constituent is rewritten as

$$\operatorname{div}(-n^F p \mathbf{I}) + n^F \rho^{FR} \mathbf{b} + p \operatorname{grad} n^F - \mathbf{H}^F \mathbf{w}_{FR} = \mathbf{0}, \quad (30)$$

which can be rearranged to explicitly determine the seepage velocity \mathbf{w}_{FR} . Finally, using the relation between the fluid filter velocity and the seepage velocity, $\mathbf{w}_F = n^F \mathbf{w}_{FR}$, the fluid filter velocity is obtained as

$$\mathbf{w}_F = [n^F]^2 [\mathbf{H}^F]^{-1} [-\operatorname{grad} p + \rho^{FR} \mathbf{b}]. \quad (31)$$

2.1.4 Permeability

Following the work of Berger et al. (2017), the positive definite material parameter tensor \mathbf{H}^F is defined as

$$\mathbf{H}^F = [n^F]^2 k^{-1} \mathbf{I}, \quad (32)$$

where k is the hydraulic permeability. The permeability k of the tissue is assumed to be strain dependent, which is proposed by Van der Voet (1997) as

$$k = k_0 \left[\frac{1+e}{1+e_0} \right]^M, \quad (33)$$

where k_0 and e_0 are the initial permeability and initial void ratio at zero strain, e is the void ratio in the current configuration and M is a positive constant. The void ratio e is defined as

$$e = \frac{dv^F}{dv^S}. \quad (34)$$

By combining Eqs. (2), (3), (33) and (34), the permeability k in the current configuration is derived as being associated with the volume fraction of fluid n^F in the current configuration

$$k = \beta [1 - n^F]^{-M}, \quad (35)$$

where β is a constant related to the initial permeability k_0 and initial void ratio e_0 at zero strain. Therefore, the increase in the fluid volume fraction induces the increase in the permeability and vice versa.

2.2 Damage initiation and evolution laws

The thermodynamic force Y^S is conjugated to the damage variable d and can be derived from Eq. (21) as

$$Y^S = -\rho^S \frac{\partial \psi^S}{\partial d}. \quad (36)$$

In order to derive the damage evolution law and determine the initiation criterion of damage, a damage potential function $F_{\text{dam}}^S = F_{\text{dam}}^S(Y^S, d)$ is defined for describing the damage process. According to the maximum dissipation principle, the damage evolution equation is expressed as

$$\dot{d} = \dot{\eta} \frac{\partial F_{\text{dam}}^S}{\partial Y^S}, \quad (37)$$

where the damage multiplier $\dot{\eta}$ is non-negative under loading/unloading conditions according to the Kuhn–Tucker relations

$$\begin{cases} \dot{\eta} > 0, & \text{if } F_{\text{dam}}^S = 0, \\ \dot{\eta} = 0, & \text{if } F_{\text{dam}}^S < 0. \end{cases} \quad (38)$$

In the case of damage growth, the damage multiplier $\dot{\eta}$ is determined by the damage consistency condition, $\dot{F}_{\text{dam}}^S = 0$.

2.3 Continuum damage model for PG matrix

From the structural point of view, the PG matrix provides support for the multidirectionally embedded collagen fibrils. The main mechanical function of the highly hydrated PG matrix is to resist compressive loading on AC. In addition, the intrinsic viscoelasticity of PG matrix has been proved to be of importance for the time-dependent response of AC (García and Cortés 2007). In order to describe the deformation and damage behaviours of the PG matrix, a poro-visco-hyperelastic damage model is proposed. Here, the standard Zener model is employed to capture the deformation behaviour of the PG matrix. Following the work of Bluhm (2002) and Pierce et al. (2013), the Helmholtz free energy function of the PG matrix $\psi_{\text{eq}}^{S_m}$, which considers the compaction effect, is written as

$$\begin{aligned} \psi^{S_m}(\mathbf{C}_{S_m}, d_m, \boldsymbol{\Gamma}^{S_m}) = & [1 - d_m] \psi_{\text{eq}0}^{S_m}(J_{S_m}, I_{\mathbf{C}_{S_m}}) \\ & + \psi_{\text{neq}}^{S_m}(\mathbf{C}_{S_m}, \boldsymbol{\Gamma}^{S_m}) \end{aligned} \quad (39)$$

Here, d_m is the damage variable of the solid phase of the PG matrix. It is noted that the symbol S_m in the superscript or subscript of a quantity indicates that the quantity is related to the solid phase of the PG matrix. The damage-free Helmholtz free energy for the equilibrium state is defined as

$$\begin{aligned} \psi_{\text{eq}0}^{S_m} = & \frac{1}{\rho_{0S}^{S_m}} \left[\lambda_{cp} \left[\frac{1}{2} [\ln J_{S_m}]^2 + \xi \right] \right. \\ & \left. - \mu \ln J_{S_m} + \frac{1}{2} \mu \left[I_{\mathbf{C}_{S_m}} - 3 \right] \right], \end{aligned} \quad (40)$$

with $\rho_{0S}^{S_m}$ the partial density of the solid phase of the PG matrix in the reference configuration and $I_{\mathbf{C}_{S_m}}$ the first invariant of \mathbf{C}_{S_m} . Despite that the solid skeleton is assumed to be intrinsically incompressible, the PG matrix is compressible due to the flow of interstitial liquid through the boundaries of the system. Therefore, the change of the volume of the biphasic mixture is allowed. This change is characterized by the determinant J_{S_m} of the deformation gradient \mathbf{F}_{S_m} and is related to the volume fraction by

$$n_{0S}^{S_m} = J_{S_m} n^{S_m}, \quad (41)$$

where $n_{0S}^{S_m}$ and n^{S_m} are the volume fraction of the solid phase of the PG matrix in the reference configuration and current configuration, respectively. At the compaction point, all fluid flows out and $n^{S_m} = 1$, $J_{cp} = n_{0S}^{S_m}$. The abbreviation ξ in (40) is defined as

$$\begin{aligned} \xi = & J_{cp} \ln J_{S_m} + \frac{1 - J_{cp}}{J_{cp} - 2} \left[\ln \frac{J_{cp} - J_{S_m}}{J_{S_m} [J_{cp} - 1]} - J_{cp} \right. \\ & \left. - \ln [1 - J_{cp}] \right]. \end{aligned} \quad (42)$$

The material parameter λ_{cp} in Eq. (40)₁ is proportional to the Lamé constant λ and is defined as

$$\lambda_{cp} = \lambda \left[1 + J_{cp} \left[1 + \frac{J_{cp}^2}{1 - J_{cp}} \right] \right]^{-1}. \quad (43)$$

In Eqs. (39) and (43), the shear modulus μ and Lamé constant λ are macroscopic material parameters of the solid skeleton, which are, respectively, related to the Young's modulus E and Poisson's ratio ν by the relations

$$\mu = \frac{E}{2[1 + \nu]}, \quad \lambda = \frac{Ev}{[1 + \nu][1 - 2\nu]}. \quad (44)$$

The effective solid stress $\mathbf{T}_E^{S_m}$ in the PG matrix is derived from Eqs. (24) and (39) and decoupled into two components

$$\mathbf{T}_E^{S_m} = [1 - d_m] \mathbf{T}_{E,\text{eq}0}^{S_m} + \mathbf{T}_{E,\text{neq}}^{S_m}. \quad (45)$$

According to Eq. (25), the damage-free equilibrium stress $\mathbf{T}_{E,\text{eq}0}^{S_m}$ and the non-equilibrium stress $\mathbf{T}_{E,\text{neq}}^{S_m}$ are, respectively, defined as

$$\begin{aligned} \mathbf{T}_{E,\text{eq}0}^{S_m} = & \rho^{S_m} \mathbf{F}_{S_m} \left[\left[\lambda_{cp} [\ln J_{S_m} + \xi] - \mu \right] \mathbf{C}_{S_m}^{-1} + \mu \mathbf{I} \right] \mathbf{F}_{S_m}^T \\ = & J_{S_m}^{-1} \mathbf{F}_{S_m} \mathbf{S}_{\text{eq}0}^{S_m} \mathbf{F}_{S_m}^T, \\ \mathbf{T}_{E,\text{neq}}^{S_m} = & \rho^{S_m} \mathbf{F}_{S_m} \left[\int_0^t \gamma_m \exp \left[-\frac{t-s}{\tau_m} \right] \mathbf{S}_{\text{eq}0}^{S_m}(s) ds \right] \mathbf{F}_{S_m}^T \\ = & J_{S_m}^{-1} \mathbf{F}_{S_m} \mathbf{S}_{\text{neq}}^{S_m} \mathbf{F}_{S_m}^T, \end{aligned} \quad (46)$$

where ρ^{S_m} is the partial density of the solid phase of the PG matrix in the current configuration and $\mathbf{S}_{\text{eq}0}^{S_m} = 2\rho_{0S}^{S_m} \frac{\partial \psi_{\text{eq}0}^{S_m}}{\partial \mathbf{C}_{S_m}}$ is the damage-free equilibrium second Piola–Kirchhoff stress in the PG matrix. The term ξ in Eq. (46) is derived by

$$\xi = J_{S_m} \frac{\partial \xi}{\partial J_{S_m}} = J_{cp} \left[1 - \frac{J_{S_m}}{J_{S_m}^2 + \frac{J_{cp}^2}{1 - J_{cp}} [J_{S_m} - 1]} \right]. \quad (47)$$

Based on Eqs. (36) and (39), the damage driving force Y^{S_m} for the PG matrix reads

$$Y^{S_m} = -\rho^{S_m} \frac{\partial \psi^{S_m}}{\partial d_m} = \rho^{S_m} \psi_{eq0}^{S_m}. \quad (48)$$

The damage potential is proposed to be expressed as (Ma et al. 2016a)

$$\begin{aligned} F_{dam}^{S_m} &= Y^{S_m} - Z^{S_m}(d_m) \\ &= Y^{S_m} - \left[Y_0^{S_m} + \frac{Y_0^{S_m}}{b^{S_m}} \ln \left[\frac{d_{cri}}{d_{cri} - d_m} \right] \right]. \end{aligned} \quad (49)$$

Here, Z^{S_m} is the damage resistance of material. $Y_0^{S_m}$ is the initial resistance to the damage, and b^{S_m} is a model parameter controlling the evolution rate of damage resistance. d_{cri} denotes the critical value of damage. Hence, d_m accumulates from 0, intact tissue, to d_{cri} , critical state of damage in tissue ($d_{cri} = 1$ in the present work). The damage evolution law is simplified as

$$\dot{d}_m = \eta \frac{\partial F_{dam}^{S_m}}{\partial Y^{S_m}} = \dot{\eta} \quad (50)$$

In the case of damage growth, the damage rate \dot{d}_m is determined by the damage consistency condition

$$\begin{aligned} \dot{F}_{dam}^{S_m} &= \frac{\partial F_{dam}^{S_m}}{\partial Y^{S_m}} \dot{Y}^{S_m} + \frac{\partial F_{dam}^{S_m}}{\partial Z^{S_m}} \frac{\partial Z^{S_m}}{\partial d_m} \dot{d}_m = 0, \\ \Rightarrow \dot{Y}^{S_m} &= \frac{\partial Z^{S_m}}{\partial d_m} \dot{d}_m \end{aligned} \quad (51)$$

By inserting the damage resistance function Z^{S_m} , Eq. (51) becomes

$$\dot{Y}^{S_m} = \frac{Y_0^{S_m}}{b^{S_m}} \frac{1}{d_{cri} - d_m} \dot{d}_m. \quad (52)$$

According to the damage evolution law Eq. (50) and the definition of the damage multiplier Eq. (38), the relation $F_{dam}^{S_m} = 0$ holds when damage grows. In this case, the damage d_m can be obtained by using the damage potential function Eq. (49)

$$d_m = d_{cri} \left[1 - \exp \left[-b^{S_m} \left\langle \frac{Y^{S_m}}{Y_0^{S_m}} - 1 \right\rangle \right] \right], \quad (53)$$

where $\langle \bullet \rangle$ is the Macauley bracket, i.e. $\langle \bullet \rangle = [| \bullet | + \bullet]/2$. By substituting the damage variable d_m in the term $\frac{-1}{d_{cri} - d_m}$ of Eq. (52) by Eq. (53) and rearranging the result, we obtain the damage evolution equation (Ma et al. 2016a)

$$\dot{d}_m = d_{cri} \frac{b^{S_m}}{Y_0^{S_m}} \exp \left[-b^{S_m} \left\langle \frac{Y^{S_m}}{Y_0^{S_m}} - 1 \right\rangle \right] \dot{Y}^{S_m}. \quad (54)$$

In fact, the damage evolution equation Eq. (54) can also be obtained by taking the time derivative of Eq. (53). The damage evolution law is characterized by the initial damage resistance $Y_0^{S_m}$, the damage development parameter b^{S_m} and the critical value of damage d_{cri} .

2.4 Continuum damage model for collagen fibrils

Debonding of cross-links between primary fibrils is generally believed to be the earliest change in collagen fibril network (Mansfield et al. 2015; Wilson et al. 2005). In OA cartilage, owing to the digestion effects of collagenases, the strength of the molecular chains between the primary fibrils and cross-links becomes significantly weaker than that in normal AC (Natarajan et al. 2015), which results in decreased damage resistance of fibrils. When more severe degeneration occurs, fibrillation, cleft and disintegration phenomena of collagen fibrils are observed and broken collagen fibrils are found at tips of AC cracks caused by mechanical loading (Hwang et al. 1992; Lewis and Johnson 2001). In the present work, collagen fibril is assumed to be a monoconstituent tissue. The thermomechanical framework for the constitutive modelling of single-phase solids at finite strains can be found in (Holzapfel and Gasser 2001; Peña 2011b; Ma et al. 2016b). According to the suggestion that the collagen fibrils resist mainly tensile loadings (Hosseini et al. 2014; Han et al. 2011; Wilson et al. 2005), the Helmholtz free energy density coupled with damage for collagen fibrils is decoupled to a equilibrium term and a non-equilibrium term

$$\begin{aligned} \psi^{cf}(\mathbf{C}_{cf}, d_{cf}, \Gamma^{cf}) &= H(T_h^{cf}) \left[[1 - d_{cf}] \psi_{eq0}^{cf}(J_{cf}, I_{\mathbf{C}_{cf}}) \right. \\ &\quad \left. + \psi_{neq}^{cf}(\mathbf{C}_{cf}, \Gamma^{cf}) \right], \end{aligned} \quad (55)$$

where $H(T_h^{cf})$ is the Heaviside function that controls the loading mode of collagen fibrils,

$$H(T_h) = \begin{cases} 1, & \text{if } T_h^{cf} \geq 0, \\ 0, & \text{if } T_h^{cf} < 0. \end{cases} \quad (56)$$

Here, T_h^{cf} is the hydrostatic stress in the current configuration, related to the Cauchy stress tensor \mathbf{T}_E^{cf} as $T_h^{cf} = \frac{1}{3} \mathbf{T}_E^{cf} \cdot \mathbf{I}$. J_{cf} is the Jacobian, and $I_{\mathbf{C}_{cf}}$ is the first invariant of \mathbf{C}_{cf} . d_{cf} is the damage variable of the collagen fibrils. It is noted that cf in the superscript or subscript of a quantity indicates that the quantity is related to the collagen fibrils. The damage-free equilibrium energy function is defined as

$$\begin{aligned} \psi_{\text{eq}0}^{\text{cf}} = & \frac{1}{\rho_{0S}^{\text{cf}}} \left[C_3 \left[J_{\text{cf}}^2 \ln [J_{\text{cf}}^2] - J_{\text{cf}}^2 + 1 \right] \right. \\ & \left. + \frac{C_1}{2C_2} \left[\exp [C_2 [I_{\text{cf}} - 3]^2] - 1 \right] \right], \end{aligned} \quad (57)$$

where ρ_{0S}^{cf} is the partial density of the collagen fibrils in the reference configuration. C_1 and C_2 are material parameters. C_1 is a stress-like quantity with the dimension of stresses. C_2 is dimensionless and controls the nonlinear behaviour of the function at the equilibrium state. C_3 is the bulk modulus, which is related to the Young's modulus E and Poisson's ratio ν by the relation

$$C_3 = \frac{E}{3[1-2\nu]}. \quad (58)$$

Similar to the structure of Eqs. (24) and (25), the Cauchy stress for collagen fibril \mathbf{T}_E^{cf} is written as

$$\mathbf{T}_E^{\text{cf}} = H(T_h^{\text{cf}}) \left[[1 - d_{\text{cf}}] \mathbf{T}_{E,\text{eq}0}^{\text{cf}} + \mathbf{T}_{E,\text{neq}}^{\text{cf}} \right], \quad (59)$$

where the damage-free equilibrium stress $\mathbf{T}_{E,\text{eq}0}^{\text{cf}}$ and the non-equilibrium viscous stress $\mathbf{T}_{E,\text{neq}}^{\text{cf}}$ are, respectively, defined as

$$\begin{aligned} \mathbf{T}_{E,\text{eq}0}^{\text{cf}} = & \rho^{\text{cf}} \mathbf{F}_{\text{cf}} \left[2C_3 J_{\text{cf}}^2 \ln [J_{\text{cf}}^2] \mathbf{C}_{\text{cf}}^{-1} \right. \\ & \left. + 2C_1 \exp \left[C_2 [I_{\text{cf}} - 3]^2 \right] \left[I_{\text{cf}} - 3 \right] \mathbf{I} \mathbf{F}_{\text{cf}}^T \right] \\ = & J_{\text{cf}}^{-1} \mathbf{F}_{\text{cf}} \mathbf{S}_{\text{eq}0}^{\text{cf}} \mathbf{F}_{\text{cf}}^T, \end{aligned} \quad (60)$$

$$\begin{aligned} \mathbf{T}_{E,\text{neq}}^{\text{cf}} = & \rho^{\text{cf}} \mathbf{F}_{\text{cf}} \left[\int_0^t \gamma_{\text{cf}} \exp \left[-\frac{t-s}{\tau_{\text{cf}}} \right] \dot{\mathbf{S}}_{\text{eq}0}^{\text{cf}}(s) ds \right] \mathbf{F}_{\text{cf}}^T \\ = & J_{\text{cf}}^{-1} \mathbf{F}_{\text{cf}} \mathbf{S}_{\text{neq}}^{\text{cf}} \mathbf{F}_{\text{cf}}^T, \end{aligned}$$

where ρ^{cf} is the partial density of the collagen fibrils in the current configuration and $\mathbf{S}_{\text{eq}0}^{\text{cf}} = 2\rho_{0S}^{\text{cf}} \frac{\partial \psi_{\text{eq}0}^{\text{cf}}}{\partial C_{\text{cf}}}$ is the damage-free equilibrium second Piola-Kirchhoff stress in collagen fibrils. The damage driving force that is evolving the damage process is derived in analogy to Eqs. (36) and (55) and is written in the form

$$Y^{\text{cf}} = -\rho^{\text{cf}} \frac{\partial \psi^{\text{cf}}}{\partial d^{\text{cf}}} = \begin{cases} \rho^{\text{cf}} \psi_{\text{eq}0}^{\text{cf}}, & \text{if } T_h^{\text{cf}} \geq 0, \\ 0, & \text{if } T_h^{\text{cf}} < 0. \end{cases} \quad (61)$$

In order to derive the damage evolution equation for collagen fibrils, the same approach for the PG matrix (Eqs. 49–54) is applied to collagen fibrils by replacing the damage driving force Y^{S_m} of the PG matrix with the damage driving force Y^{cf} of collagen fibrils presented in Eq. (61). The damage evolution equation for collagen fibrils is derived as

$$\dot{d}_{\text{cf}} = d_{\text{cri}} \frac{b^{\text{cf}}}{Y_0^{\text{cf}}} \exp \left[-b^{\text{cf}} \left(\frac{Y^{\text{cf}}}{Y_0^{\text{cf}}} - 1 \right) \right] \dot{Y}^{\text{cf}}, \quad (62)$$

where Y_0^{cf} is the initial resistance to the damage, b^{cf} is a model parameter controlling the evolution rate of damage resistance and d_{cri} denotes the critical value of damage. Hence, d_{cf} accumulates from 0, intact collagen fibrils, to d_{cri} . The above constitutive equations for collagen fibrils enable the 3D geometrical modelling of the collagen fibrils using continuum elements in the simulation. In order to reduce the computation time, the constitutive equations can be simplified for 1D cases, where the collagen fibrils are discretized by using truss elements in the simulation.

2.5 Nonlocal averaging algorithm for continuum damage model

The integral-type nonlocal average algorithm is an effective approach to eliminate the spurious mesh dependency in the damage modelling of soft tissues involving strain softening (Andrade et al. 2014; Fathi et al. 2017; Ferreira et al. 2017). In addition to the integral-type nonlocal formulation, other available approaches for avoiding mesh dependency mainly include the viscous regularization methods (Peña 2011a), relaxed incremental variational formulation (Balzani and Ortiz 2012) and nonlocal gradient-enhanced formulation (Waffenschmidt et al. 2014). In the present study, the integral-type nonlocal damage averaging algorithm is adopted to compute the non-local damage driving forces Y_*^ρ ($\rho = S_m, \text{cf}$). The resulting equivalent quantity Y_*^ρ will be used to replace the corresponding local damage driving force Y^ρ . The nonlocal approach supposes that the material response at a certain point depends not only on the state of that point itself but also on the state of material points within the neighbourhood of that point. The nonlocal variable $Y_*^{S_m}$ and Y_*^{cf} for PG matrix and collagen fibril, respectively, represents the equivalent damage driving force at a material point ζ , averaged over a spherical search zone with a certain nonlocal volume V^{nl} . The spherical search zone (V^{nl}) is defined by a material characteristic length l_r centred at the material point ζ to surround a set of neighbouring points ϑ . The nonlocal averaging of the damage driving force Y_*^ρ at a given spatial material point ζ is defined as

$$Y_*^\rho(\zeta) = \int_{V^{\text{nl}}} \omega(\zeta, \vartheta) Y^\rho(\vartheta) dV^{\text{nl}}(\vartheta), \quad (63)$$

where Y_*^ρ and Y^ρ denote the average equivalent nonlocal quantity and the corresponding local quantity, respectively. $\omega(\zeta, \vartheta)$ is an averaging operator, defined by

$$\omega(\zeta, \vartheta) = \frac{\xi(\|(\zeta - \vartheta)\|)}{\int_{V^{\text{nl}}} \xi(\|(\zeta - \vartheta)\|) dV^{\text{nl}}(\vartheta)}, \quad (64)$$

where the integration variable $\boldsymbol{\varpi}$ represents the location of an arbitrary material point within the defined finite volume V^n and ξ denotes a weighting function. Here, we adopt a extensively used bell-shaped weighting function (Andrade et al. 2011), which is given by

$$\xi(\|(\boldsymbol{\zeta} - \boldsymbol{\varpi})\|) = \left\langle 1 - \frac{\|(\boldsymbol{\zeta} - \boldsymbol{\varpi})\|^2}{l_r^2} \right\rangle^2, \quad (65)$$

where $\langle \cdot \rangle$ is the Macauley bracket as defined in Sect. 2.3, i.e. $\langle \cdot \rangle = [| \cdot | + \cdot]/2$.

In a case of small deformation, the nonlocal averaging does not depend on the configuration since the difference between the reference and the deformed configurations can be neglected. In this case, Eqs. (63)–(65) remain constant during the simulation according to the postulation of Jirásek (2007). However, for finite deformation problems, the relative distance between Gaussian points may change considerably, giving rise to apparent change of the averaging operator in Eq. (64). Therefore, three different nonlocal averaging strategies were postulated, i.e. total Lagrangian type, updated Lagrangian type and Eulerian type (Fathi et al. 2017; Andrade et al. 2011). In the total Lagrangian type algorithm, the candidate Gaussian points $\boldsymbol{\vartheta}$ within the spherical search zone and the relative distances between these candidate Gaussian points and the reference point $\boldsymbol{\zeta}$ are predetermined in the initial configuration before the analysis and remain constant during the simulation. In the updated Lagrangian type algorithm, the locations of the predetermined candidate Gaussian points are updated in the current configuration and the corresponding averaging operator is recomputed. The Eulerian type algorithm also updates the search zone, which is characterized by the characteristic

length l_r , at each analysis step to redetermine the Gaussian points within the spherical search zone in the current configuration. Noticeably, when the total Lagrangian type averaging strategy is utilized, the averaging operator ω merely needs to be evaluated once, while in the other two averaging strategies, the averaging operator ω has to be computed at every analysis step. From a computational point of view, the total Lagrangian type strategy can significantly reduce computational time in comparison with the other two ones (Andrade et al. 2011). In addition, a previous study showed that all these three strategies caused regularized solutions (Andrade et al. 2011). Therefore, the total Lagrangian type nonlocal strategy is used in the present study in order to reduce the computational time in the 3D simulations.

The biphasic visco-hyperelastic damage model is implemented in the commercial software Abaqus/Standard (Version 2017, Dassault Systèmes Simulia Corp., Johnston, RI, USA) via the user material subroutine UMAT. The nonlocal damage driving force is updated during FE computation in Abaqus/Standard via the user subroutine UEXTERNALDB. The numerical algorithm for the constitutive model of the PG matrix is summarized in Table 1. A similar numerical algorithm without considering the behaviour of the fluid constituent is applied to the constitutive model of collagen fibrils.

3 Parameter study of the nonlocal averaging algorithm

In order to verify the mesh independence of the constitutive model, a 3D porous hollow cylindrical model with a rounded notch is used in the simulation. The constitutive model for

Table 1 Numerical algorithm for the FE-implementation of the constitutive model of the PG matrix

```

Initialize all variables:  $\mathbf{u}_S$ ,  $p$ ,  $n^F$ 
WHILE  $t < T$  DO (Time stepping loop)
  WHILE  $\|\mathbf{R}\| > \text{TOL}$  DO (Non-linear solution loop)
    (I) Calculate the effective solid stresses
      (i) Calculate the deformation gradient tensor of the solid phase  $\mathbf{F}_{S_m}$  from  $\mathbf{u}_S$ 
      (ii) Compute the equilibrium second Piola-Kirchhoff stress  $\mathbf{S}_{eq0}^{S_m}$  and Cauchy stress  $\mathbf{T}_{E,eq0}^{S_m}$  (Eq.(46))
      (iii) Compute the non-equilibrium second Piola-Kirchhoff stress  $\mathbf{S}_{neq}^{S_m}$  and Cauchy stress  $\mathbf{T}_{E,neq}^{S_m}$  (Eq.(46))
    (II) Calculate the damage variable  $d_m$ 
      (i) Compute the local damage driving force  $Y^{S_m}$  (Eq.(48))
      (ii) Compute the nonlocal damage driving force  $Y_*^{S_m}$  (Eq.(63))
      (iii) Check the damage criterion
        IF  $Y_*^{S_m} > Y_0^{S_m}$  THEN
          Update the damage variable  $d_m$  using the damage evolution equation Eq.(54)
        END IF
    (III) Update effective solid Cauchy stresses (Eq.(45))
    (IV) Calculate the material Jacobian tensor
    (V) Store internal variables  $\mathbf{S}_{neq}^{S_m}$ ,  $\mathbf{S}_{eq0}^{S_m}$ ,  $d_m$  and  $Y_*^{S_m}$ 
    (VI) Update  $n^{S_m}$ ,  $n^F$ ,  $\rho^{S_m}$  and  $\rho^F$ 
       $n^{S_m} = n_{0S}^{S_m} [\det \mathbf{F}_{S_m}]^{-1}$ ,  $n^F = 1 - n^{S_m} = 1 - n_{0S}^{S_m} [\det \mathbf{F}_{S_m}]^{-1}$ 
       $\rho^{S_m} = n^{S_m} \rho^{SR}$ ,  $\rho^F = n^F \rho^{FR}$ 
    (VII) Calculate the permeability based on Eq.(35)
    (VIII) Calculate the fluid pore pressure  $p$  and the solid displacement vector  $\mathbf{u}_S$  by solving the weak form of Eq.(10), Eq.(11) and Eq.(31)
  END WHILE
  Update time step  $t = t + \Delta t$ 
END WHILE

```

R: Residual vectors for Newton iterations; TOL: Convergence tolerance for Newton iterations

the PG matrix is implemented via the UMAT subroutine in Abaqus Standard. The length, inner radius and outer radius of the specimen are 16 mm, 3 mm and 6 mm, respectively. The radius of the notch is 1.5 mm, located at the centre of the notched specimen. Due to symmetry, simulations are performed using one eighth model of the notched specimen to reduce computation time (Fig. 1). Symmetry boundary conditions are applied to the cross-sectional surfaces. Free-draining boundary conditions are applied to the inner and outer cylindrical surfaces by setting the pore pressure to zero. Fluid flow is not allowed across other surfaces. An axial displacement along the z -axis at a loading rate of 0.01 mm/s is applied to the upper surface. The simulation is terminated when the convergence issue arises in the solution procedure of the nonlinear equation system using the Newton–Raphson method. The material parameters for the notched specimen are shown in Table 2.

3.1 Effect of element size

In order to assess the mesh sensitivity of the numerical results, three meshes were used, which consist of 48,360, 15,132 and 5776 8-node linear stress/pore pressure-reduced integration elements (C3D8RP), respectively. Sizes of elements at the notched zone of the three models are 0.1 mm, 0.15 mm and 0.2 mm, respectively. To obtain a mesh-independent solution, enough integration points should lie within the averaging volume. An material characteristic length l_r

of 0.3 mm is used to include up to 194, 64 and 25 elements into the averaging volume for three meshes, respectively. Additionally, the simulation results using local damage models are also presented to allow a comparison with the nonlocal damage modelling. Damage contours of the three notched models without and with nonlocal regularization are illustrated in Fig. 2a–c and d–f, respectively. Damage distributions from the simulation results without the nonlocal regularization are significantly influenced by the mesh densities. The damage in all nonlocal models locates at the same region with almost the same size (Fig. 2d–f), eliminating the mesh dependency.

The axial force–displacement curves from the simulations with and without nonlocal damage averaging algorithm are shown in Fig. 3a. The reaction force curves of the local models overlap in the ascending periods until the forces begin to fall due to damage progressions. The difference of mesh density in the local models causes the dispersion of the three local forces. By contrast, the nonlocal simulation results confirm that the mesh dependency becomes insignificant by using the nonlocal damage averaging algorithm.

3.2 Effect of characteristic length l_r

The notched model with element size of 0.15 mm is used to analyse the influence of the characteristic length l_r on the simulation results. Four characteristic length l_r of 0.2 mm, 0.3 mm, 0.45 mm and 0.8 mm are specified to include

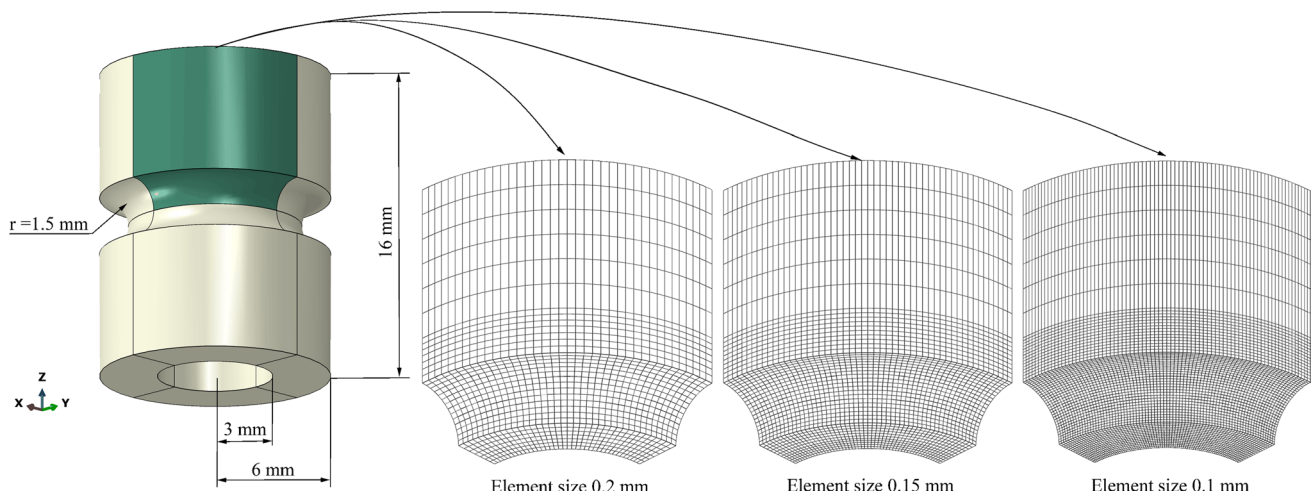


Fig. 1 Geometry of the notched specimen with different meshes. Due to symmetric conditions, one eighth of the notched specimen is used in simulations. Three different meshes consist of 5776, 15,132 and

48,360 elements, respectively. The element size of the corresponding meshes in the notch region is 0.2 mm, 0.15 mm and 0.1 mm, respectively

Table 2 Material parameters for the notched specimen in the simulation

μ (MPa)	λ (MPa)	$Y_0^{S_m}$ (mJ/mm ³)	b^{S_m} (-)	n_{0S}^F (-)	J_{cp} (-)	β (mm ⁴ /N s)	M (-)	τ_m (s)	γ_m
0.3391	0.1453	0.0422	3.3338	0.8014	0.2588	5.127×10^{-5}	1.339	1050	1.0

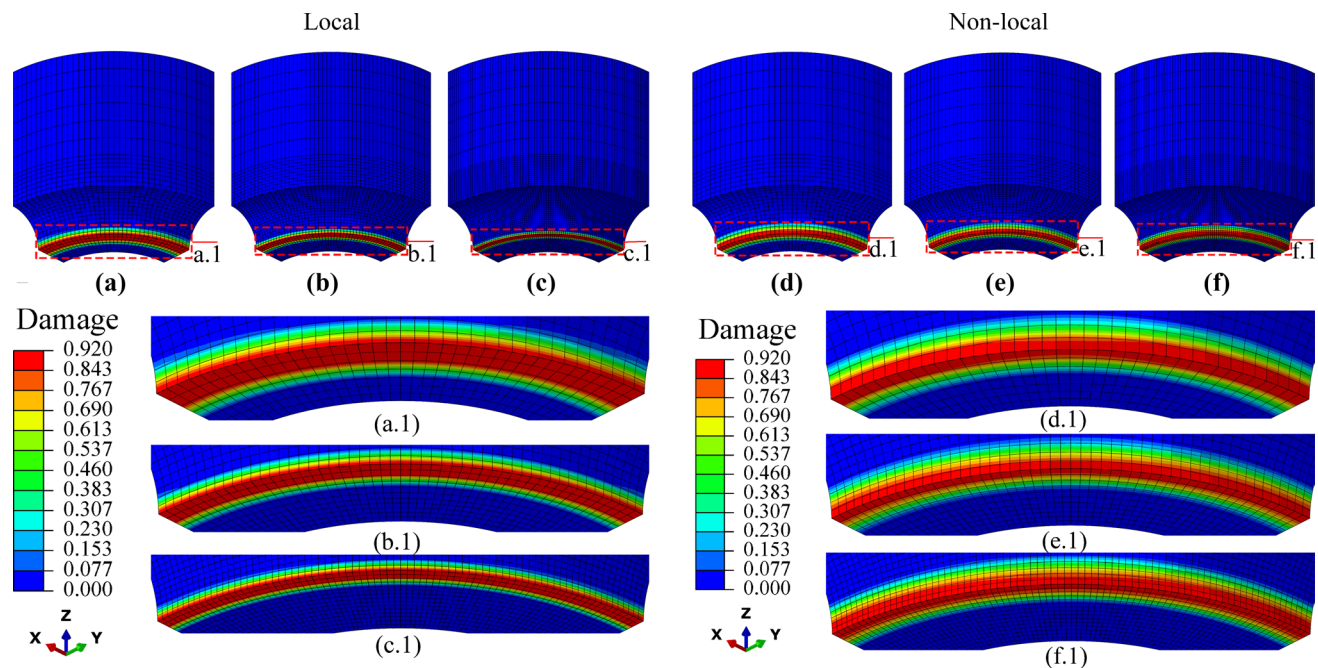


Fig. 2 Damage distributions in the notched specimens computed using the local and nonlocal damage models. **a** The local damage model with the element size of 0.2 mm. **b** The local model with the element size of 0.15 mm. **c** The local damage model with the element size of 0.1 mm. **d** The nonlocal damage model with the element size

of 0.2 mm. **e** The nonlocal damage model with the element size of 0.15 mm. **f** The nonlocal damage model with the element size of 0.1 mm. The partially enlarged views of the marked zones in (a)–(f) are shown in (a.1)–(f.1), respectively

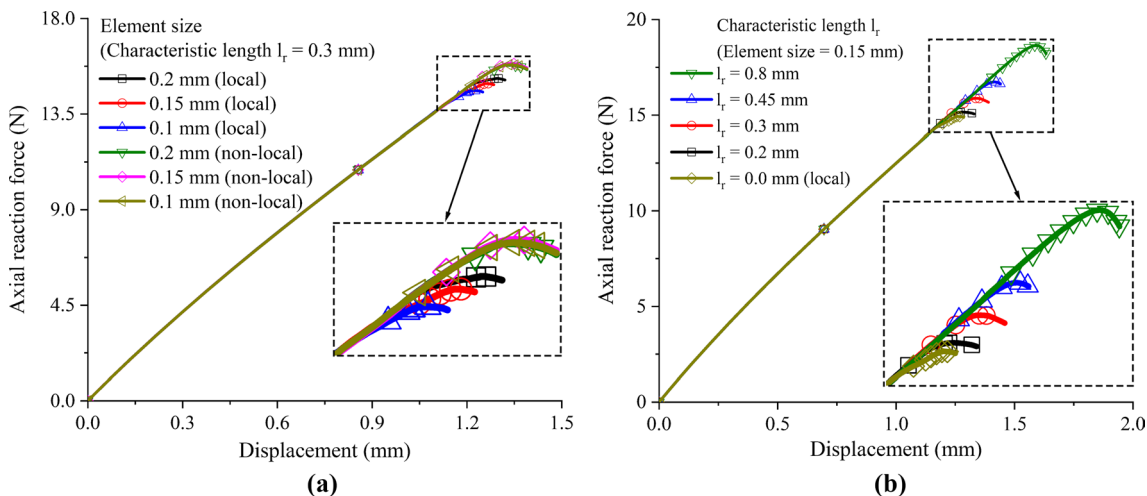


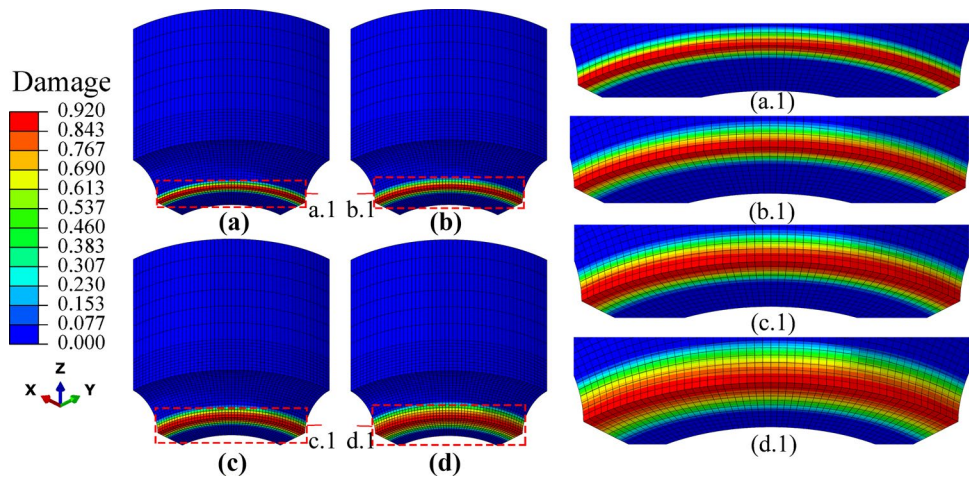
Fig. 3 Axial force–displacement curves of the notched model under axial tension. **a** Simulation results using different meshes for local and nonlocal damage models. **b** Effects of the characteristic length l_r

23, 64, 179 and 771 elements into the averaging volume, respectively. The influence of the characteristic length on the damage distributions is shown in Fig. 4. It is seen that the increase in the characteristic length leads to an increase in the damaged region size in the radial and axial directions.

on the simulation results. Simulations are terminated when convergence issue arises during the softening stage

Figure 3b presents the forces–displacement curves obtained from the simulations with different characteristic lengths. The load-bearing capability is higher when a larger characteristic length is specified. It should be noted that if the characteristic length is too large, the damage evolution can be overhomogenized.

Fig. 4 Damage distributions of the simulations with different material lengths l_r . **a** $l_r = 0.2 \text{ mm}$. **b** $l_r = 0.3 \text{ mm}$. **c** $l_r = 0.45 \text{ mm}$. **d** $l_r = 0.8 \text{ mm}$. The partially enlarged views of the marked zones in (a–d) are shown in (a.1–d.1), respectively



4 3D micromechanical modelling for articular cartilage

4.1 Geometrical models

The aim of the present work is to study the influence of OA-induced microstructural and compositional changes on the mechanical and damage behaviour of AC. In the computational simulations, three microstructural models are built to represent the normal, early OA and moderately advanced osteoarthritic AC samples, respectively (Fig. 5). Geometrical parameters of the microstructural models in this study are according to the experimental measurement

of AC samples in (Henao-Murillo et al. 2018). The samples include a layer of AC, the underlying calcified cartilage (CC) and subchondral bone (SCB). The thickness and radius of the AC samples are 6 mm and 3.75 mm, respectively. The 1.05-mm-thick AC layer is divided into the aforementioned three layers, i.e. SZ, MZ and DZ layers, distinguished by the predominant orientations of collagen fibrils as mentioned in Sect. 1. The thickness of SZ, MZ and DZ layers is 0.2 mm, 0.45 mm and 0.4 mm, respectively (Antons et al. 2018; Gottardi et al. 2016; Sophia Fox et al. 2009). The thickness of CC is 0.15 mm, and the underlying substrate is modelled as SCB (Lane and Bullough 1980). In addition, in order to identify the viscoelastic parameters of AC, a different AC sample used in

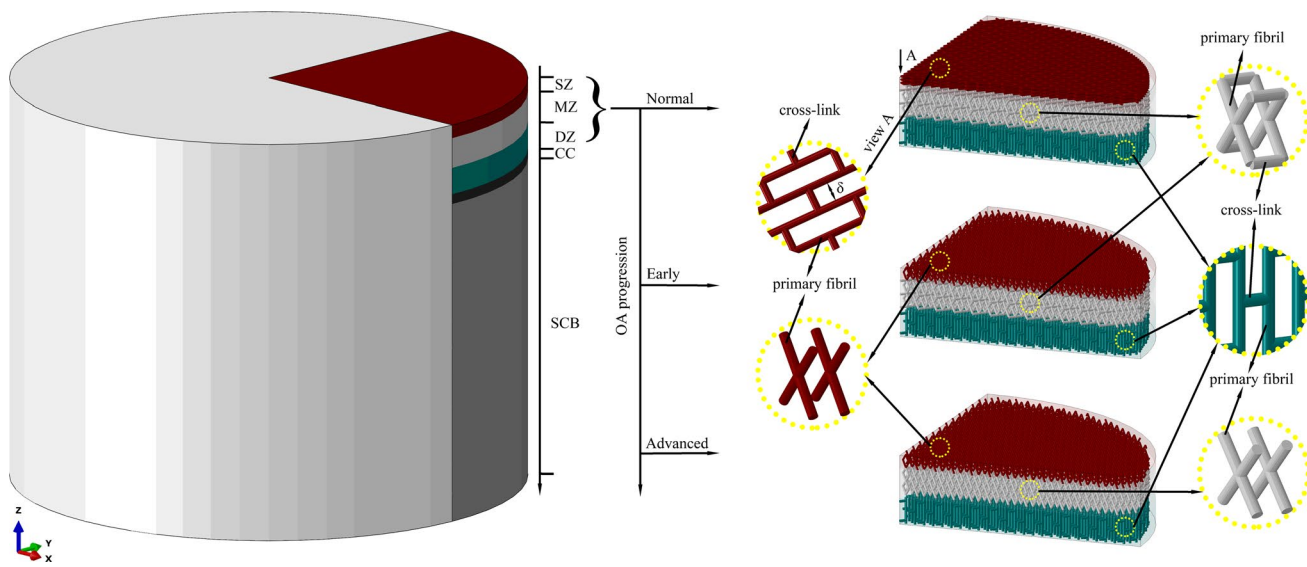


Fig. 5 Microstructural models of cylindrical specimens of AC with different degrees of OA. A quarter of the AC model is used in the simulations due to symmetry conditions. The symbols SZ, MZ, DZ, CC and SCB are labelled to the graphs to distinguish distinct layers.

The partially enlarged details of the microstructure of the collagen fibril networks in every zone are illustrated to clarify the change of the fibril networks with the progression of OA

the stress-relaxation experiment of (Julkunen et al. 2008) is built for the computational simulation, where the CC and SCB are not included as reported in the experimental study. The thickness and radius of the sample are 2.32 mm and 2 mm, respectively. The ratio between the thickness of SZ, MZ and DZ, as well as the structure of fibril networks, is identical to that of the early OA model in Fig. 5.

In the normal AC model, primary collagen fibrils in the SZ layer are parallel to AC surface, orient at +45° and −45° to the AC surface in the MZ layer and direct perpendicularly to the subchondral bone surface in the DZ layer (Wilson et al. 2006a). According to the microscopic investigations (Canty 2005), short telopeptides locating at either end of a large collagen fibril assemble into highly ordered, string-like transverse cross-links. Therefore, we assume that cross-links are modelled by short fibrils, which are located between primary fibrils. Cross-links orient perpendicularly to the axes of primary fibrils, which transversely connect two neighbouring primary fibrils. In addition, microstructural studies of collagen fibrils network show that the ratio between the length of type II collagen and the interfibrillar space is about 3:1 (Han et al. 2011). In the present work, the macroscopic sizes of the samples in the simulation involving SZ, MZ and DZ layer are much larger than the nanoscale dimensions of collagen fibrils. In order to reduce computation time, the length of a cross-link is equal to the interfibrillar space $\delta = 0.1$ mm, while a single primary fibril is modelled as a truss segment with the unit length of 0.3 mm. According to different volume fractions of fibrils in SZ, MZ and DZ layers (Julkunen et al. 2008), the cross-sectional areas of the fibrils in every layer for different AC samples are listed in Table 3. It is noted that the proposed microstructural models cannot describe the structural features of AC at the nanoscale. During the progression of OA, the structural change of collagen fibrils initiates from the SZ layer and develops further into the DZ layer of cartilage (Saarakkala et al. 2010). In early OA, fibrils in the SZ layer are observed to be obviously disorganized, while no significant changes of fibrillar

structure are observed in the other two layers (Saarakkala et al. 2010). Therefore, in early OA sample, fibrils in SZ layer are modelled as oblique (+45° and −45° to AC surface) to represent fibrillation (Mononen et al. 2011). Structures of fibrils in other two layers are identical to that in the normal AC sample. Experimental investigations support that loosening and breakdown of cross-links between large fibrils occur in significantly degenerated cartilages (Natarajan et al. 2015; Mansfield et al. 2015). The degeneration is more pronounced in the SZ and MZ layers (Wilson et al. 2005). According to these studies, we assume that in the advanced OA samples, no cross-links exist in the SZ and MZ layer, while the structure of the collagen fibril network in the DZ layer retains intact like that in the DZ layer of the normal AC sample and the early OA cartilage sample (Mononen et al. 2011).

4.2 Material properties

Material properties of PG matrix and collagen fibrils in human AC are closely associated with age, gender, health condition and joint types. Previous experimental studies showed that the compressive modulus of AC increased significantly with depth from the articular surface (Schinagl et al. 1997) and the PG matrix in AC mainly contributed to the compressive modulus (Canal Guterl et al. 2010). Therefore, in the present study, elastic properties of PG matrix are assumed to be depth dependent, while elastic properties of collagen fibrils remain depth independent (Men et al. 2017). In the current study, Young's modulus for PG matrix and collagen fibrils in the normal AC model are from the work of Men et al. (2017). With progression of OA, collagen fibril degradation is related to the reduced elastic stiffness (Liukkonen et al. 2017). Previous studies show that fibril degradation occurs from a very early OA stage and the fibril modulus can decrease by more than 60% in the most advanced OA stage (Korhonen et al. 2003; Mononen et al. 2011). Based on these results, for considering the fibril degradation in the stages of early OA and moderately advanced OA, fibril

Table 3 Model and material parameters used in the simulation of AC with different degrees of OA. The volume fractions of the compositions in the normal AC and osteoarthritic AC models are based on previous studies by Pierce et al. (2016) and Julkunen et al. (2008), respectively

AC state	Layer	C_3 (MPa)	μ (MPa)	λ (MPa)	n_{OS}^F (−)	A_0^{cf} (mm ²)	J_{cp} (−)
Normal	SZ	5.9524	0.1577	0.0445	0.8426	6.74×10^{-4}	0.2388
	MZ	5.9524	0.3391	0.1453	0.8014	9.71×10^{-4}	0.2588
	DZ	5.9524	0.5641	0.2906	0.7338	1.27×10^{-3}	0.2761
	SZ	4.4643	0.1577	0.0445	0.9204	3.39×10^{-4}	0.2672
	MZ	4.4643	0.3391	0.1453	0.8860	4.52×10^{-4}	0.2701
	DZ	4.4643	0.5641	0.2906	0.8556	7.26×10^{-4}	0.2591
Early	SZ	2.9762	0.1577	0.0445	0.9297	1.40×10^{-4}	0.2851
	MZ	2.9762	0.3391	0.1453	0.8876	3.47×10^{-4}	0.2955
	DZ	2.9762	0.5641	0.2906	0.7982	7.57×10^{-4}	0.2980

n_{OS}^F represents the volume fraction of the fluid in the initial configuration, which is calculated by Eq. (66). A_0^{cf} denotes the cross-sectional area of the collagen fibrils in each layer in the initial configuration

moduli are assumed to be decreased by 25% and 50% of the normal fibril modulus, respectively. The parameters $C_1 = 3$ MPa and $C_2 = 8$ for fibrils are from the work by Pierce et al. (2013) and assumed to be identical in the normal and OA models. Additionally, OA-induced disruptions of collagen fibrils occur prior to PG loss (Wen et al. 2012). The PG matrix at the early and moderately advanced OA stage shows apparently intact. Substantial PG loss is mainly observed in the more advanced OA stage (Gottardi et al. 2016; Wilusz et al. 2013; Arokoski et al. 2000). Correspondingly, Young's moduli of the PG matrix in the early and the moderately advanced OA are assumed to be the same as the normal AC. The influence of OA on compositions of AC is characterized by changing the relative fraction of compositions based on the biochemical analyses of AC samples in the previous work of Julkunen et al. (2008). The depth-dependent compositional information of the normal AC model is from the study of Pierce et al. (2016). The positive material constant β and M in Eq. (35) is 5.127×10^{-5} mm⁴/N s and 1.339, respectively (Julkunen et al. 2008). In all AC models, we assume that 25% volume fraction fluid is trapped in the intrafibrillar space of collagen and cannot escape from the tissue (Pierce et al. 2013; Arokoski et al. 2000). Therefore, $J_{cp} = n_{0S}^{S_m} + 0.25n_{0S}^F$, where $n_{0S}^{S_m}$ and n_{0S}^F , respectively, denote the volume fraction of the solid and fluid constituents in the PG matrix in the initial configuration. The realistic density of the fluid and solid is assumed to be $\rho^{FR} = 1$ g/ml and $\rho^{SR} = 1.4338$ g/ml, respectively (Julkunen et al. 2008). The viscoelastic parameters $\gamma_{cf} = 2.2$ and $\tau_{cf} = 100$ s for collagen fibrils are specified based on the work of Pierce et al. (2016). The viscoelastic parameters are assumed to be not influenced by OA (Mononen et al. 2011). The damage parameters $Y_0^{S_m}$ and Y_0^{cf} , b^{S_m} and b^{cf} , as well as the viscoelastic parameters γ_m and τ_m , will be identified in next sections. Other model parameters and the compositional information are listed in Table 3. It should be noted that the volume ratio between the solid phase of the PG matrix and collagen fibrils is equal to their mass ratio, since we assume that the realistic density of the solid phase of the PG matrix and the density of fibrils are identical (Wilson et al. 2007; Julkunen et al. 2008). The initial volume fraction of fluid n_{0S}^F is derived from the initial fluid mass fraction n_{mass}^{0F} and the solid real density ρ^{SR} by the equation

$$n_{0S}^F = \frac{\rho^{SR} n_{mass}^{0F}}{1 - n_{mass}^{0F} + \rho^{SR} n_{mass}^{0F}}. \quad (66)$$

In the present work, an energy-based damage model is used as described in Sect. 2.2. However, due to lack of experimental data regarding the strain energy of damage initiation and evolution for collagen fibrils and PG matrix of AC, damage model parameters are determined according to the damage initiation and failure strains ($\epsilon_0, \epsilon_{cri}$) reported in

the literatures. The threshold and failure strains (0.08, 0.28) for collagen fibrils in normal AC are estimated by previous studies (Hosseini et al. 2014; Sophia Fox et al. 2009; Párraga Quiroga et al. 2017; Heijerjans et al. 2017). From the structural point of view, the OA-induced degeneration of collagen fibril networks mainly includes two mechanisms, i.e. the disruption of the network structure and the multi-step splitting of individual collagen fibres into prototypic fibrils (Gottardi et al. 2016). The experimental results in (Gottardi et al. 2016) show that the splitting of thick collagen fibres into prototypic subunits is more significant in cartilages with higher OA grades, indicating that the damage resistance of individual fibres decreases with the OA development. Since both mechanisms contribute to the decrease in the damage resistance of AC, they should be considered for modelling the damage behaviour of osteoarthritic cartilages. The effect of the latter degeneration mechanism of collagen fibrils on the decreased damage resistance is taken into account by reducing the threshold and failure strains of fibrils in the OA cartilage. However, to the best of our knowledge, the experimental quantification of damage strain of individual fibres in osteoarthritic AC is not available in the literature. Therefore, we assume the threshold and failure strains of early OA and advanced OA cartilage reduce to 50 % and 25 % of those for normal AC, respectively. The resulting values for the early OA and advanced OA cartilages are (0.04, 0.14) and (0.02, 0.07), respectively. The threshold and failure strains for the PG matrix, i.e. (0.3, 0.6), are also directly adopted from the literatures (Hosseini et al. 2014; Párraga Quiroga et al. 2017; Torzilli et al. 1999). Due to the aforementioned assumption that the PG matrix at the early and moderately advanced OA stage is intact, the threshold and failure strains for the PG matrix in all models are assumed to be the same. The parameters of damage model for the PG matrix and collagen fibrils are identified by matching the damage initiation and failure strains under uniaxial compression and tension, respectively, since the PG matrix primarily resists compression and fibrils are assumed to only resist tension. Parameter studies are also carried out to present the effect of these parameters on the predicted damage behaviour as shown in Fig. 6.

The damage in the SZ layer of the PG matrix initiates at strain of 0.3 when $Y_0^{S_m} = 0.0193$ mJ/mm³ and material is totally damaged at strain of 0.6 when $b^{S_m} = 3.3389$ (Fig. 6a). The corresponding values of damage parameters ($Y_0^{S_m}$ and b^{S_m}) for the PG matrix in the MZ and DZ layers are (0.0422 mJ/mm³, 3.3338) (Fig. 6b) and (0.0709 mJ/mm³, 3.3323) (Fig. 6c), respectively. Since $Y_0^{S_m}$ controls the damage initiation of the PG matrix, the increase in $Y_0^{S_m}$ results in a rise of the strain energy density, at which damage in matrix initiates. b^{S_m} is associated with the damage evolution rate of matrix. By increasing the value of b^{S_m} , damage progression in matrix significantly accelerates until b^{S_m} reaches a certain value, after which damage progresses slowly with

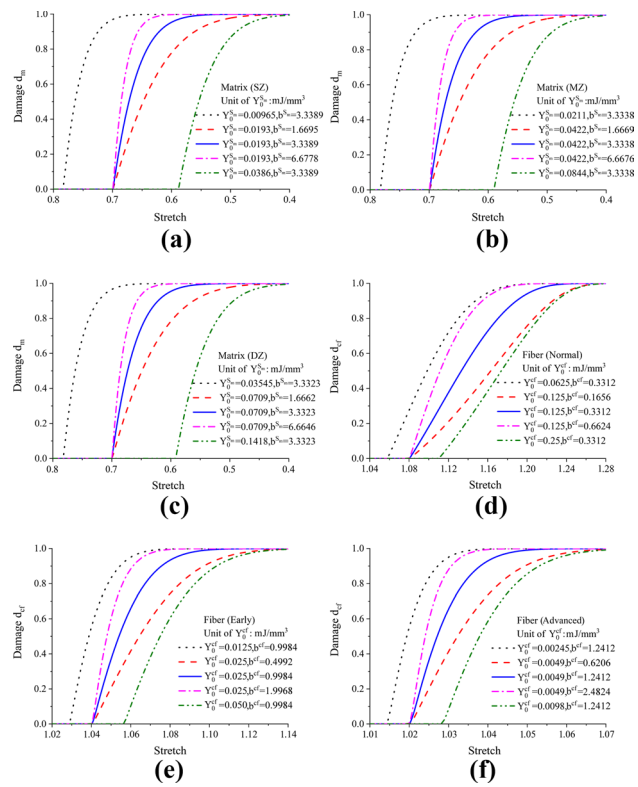


Fig. 6 Effects of damage parameters $Y_0^{S_m}$ and b^{S_m} on the damage evolution for the PG matrix in SZ, MZ and DZ are shown in (a–c), respectively. Effects of damage parameters Y_0^{cf} and b^{cf} on the damage evolution for fibrils in the normal AC, early OA model and advanced OA samples are shown in (d–f), respectively

the increase in b^{S_m} . Figure 6d–f demonstrates the damage evolution curves of collagen fibrils in the normal, early OA and advanced OA models. The values of damage parameters (Y_0^{cf} , b^{cf}) for fibrils in the normal AC, early OA cartilage and advanced OA cartilage are (0.125 mJ/mm³, 0.3312), (0.025 mJ/mm³, 0.9984) (Fig. 6e) and (0.0049 mJ/mm³, 1.2412) (Fig. 6f), respectively. The effects of Y_0^{cf} and b^{cf} on the damage behaviour of collagen fibrils are demonstrated in Fig. 6d–f.

CC and SCB are simulated by linear elastic material, with the elastic modulus of 320 MPa (Mente and Lewis 1994) and 1.15 GPa (Choi et al. 1990), respectively. Poisson's ratio for CC and SCB is both 0.3 (Stender et al. 2016). The experimental investigations of (Henao-Murillo et al. 2018) show that, under the current loading conditions, no damage is observed in the CC and SCB. Correspondingly, these two layers are not allowed to degrade in the present study.

4.3 Boundary conditions

In the present work, two loading cases are used in the simulation, namely the unconfined compression loaded

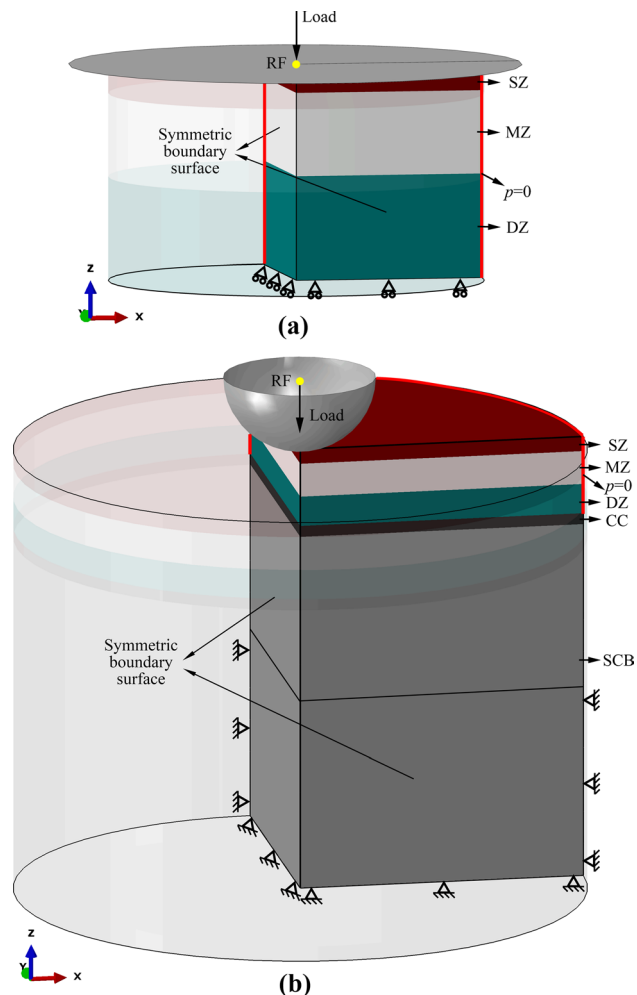


Fig. 7 Boundary conditions on the samples in **a** the unconfined compression simulation and **b** the impermeable spherical indentation simulation. A quarter of the AC model is used in the simulations due to symmetry conditions. Displacement loads are applied to the reference point (RP: the marked point on the indenter) of the rigid body plane indenter and hemispherical indenter. Symmetry boundary conditions are applied on the cross-sectional surfaces. Fluid is allowed to freely drain from the cylindrical surface of the AC layer, which is marked in the graph, by setting the pore pressure $p = 0$

with a rigid plate (Fig. 7a) and the spherical indentation compressed by a spherical indenter (Fig. 7b). The unconfined compression is conducted to identify the viscoelastic parameters (γ_m and τ_m) by comparing to available experiment data in (Julkunen et al. 2008), while the spherical indentation is performed to verify the models and parameters and to investigate the damage behaviour of AC at different OA levels. The spherical indenter is used to investigate the deformation and damage behaviour for the loading scenario with significant strain gradients and high loading rates.

4.3.1 Unconfined compression test

As illustrated in Fig. 7a, in the unconfined compression simulation, symmetry boundary conditions are applied to the cross-sectional surfaces of the numerical models. All nodes on the bottom surface of the models are constrained in the Z-axis direction. The specimen is compressed via a rigid impermeable plate. The contact between the specimen and the rigid plate is assumed to be frictionless. Free-draining boundary conditions are applied to the outer cylindrical surface by constraining the fluid pressure to be zero. The upper and lower surface is assumed to be impermeable. The loading protocol used in the unconfined compression simulation is identical to that in a previous experiment (Julkunen et al. 2008). A pre-compression of 5% of the initial AC thickness is followed by two consecutive relaxation steps. The compression depth of each relaxation step is 5% of the thickness of deformed AC. The loading velocity of the compression stages is 1 $\mu\text{m}/\text{s}$. The loading protocol of the two relaxation steps is also presented in Fig. 8a.

4.3.2 Spherical indentation test

In the spherical indentation simulation (Fig. 7b), the specimen of AC is compressed by a rigid indenter with an 1-mm-radius hemispherical tip at a loading rate of 60 mm/min. The nodes on the bottom surface and the lower half of the cylindrical surface of the SCB are constrained in all directions to

simulate the fix of the sample in experiments. Other boundary conditions are the same as that in the unconfined compression simulation.

5 Results and discussion

In order to build the models of the cartilage samples, the PG matrix and collagen fibrils are firstly modelled separately in Abaqus according to their geometry, size and fibre directions as described in Sect. 4.1. Collagen fibrils and the PG matrix are discretized by 2-node truss element (T3D2 in Abaqus) and 4-node linear tetrahedral coupled pore pressure element (C3D4P in Abaqus), respectively. In the next step, the collagen fibrils are assembled into the PG matrix. Finally, the embedded constraint method is applied to constrain the embedded nodes of fibril truss elements to degrees of freedom of the surrounding matrix element. In this study, the characteristic length l_r is specified to be 0.1 mm which is assumed to be equal to half the thickness of SZ. This value of l_r enables to include at least two layers of elements in the thickness direction (Z-axis direction) of the AC models into the nonlocal averaging zone. A mesh sensitivity analysis confirms that the mesh with element size of 0.1 mm can provide mesh-independent simulation results. The computations are carried out on workstations with 8-core Intel Xeon CPU E5-2643v0 (3.30 GHz, 64 GB RAM). The computational time for the AC samples is about 24 h.

5.1 Unconfined compression

By using the loading protocol in the experimental test (Julkunen et al. 2008) (Fig. 8a), the viscoelastic parameters $\gamma_m = 1.0$ and $\tau_m = 1050$ s are determined by fitting the computational results of the early OA model to the experimental data from the unconfined compression test, conducted on a grade 3 OA sample, by Julkunen et al. (2008) (Fig. 8b). Since only the experimental relaxation curve of the two relaxation steps was plotted in (Julkunen et al. 2008), we also only show the data of the corresponding relaxation steps. The point A in Fig. 8a, b denotes the starting point of the first relaxation step, rather than the onset of the loading protocol. As mentioned above, the viscoelastic parameters are assumed to be unaffected by the progression of OA (Mononen et al. 2011). Therefore, these identified viscoelastic parameters will also be used in the normal AC and advanced OA models.

The pore pressure gradient in the early OA specimen at the maximum axial displacement (point D in Fig. 8b) in the unconfined compression simulation is illustrated in Fig. 8c. Due to the free-draining boundary condition on the cylindrical surface of the AC model, the pore pressure on the cylindrical surface remains zero over time. Under the axial

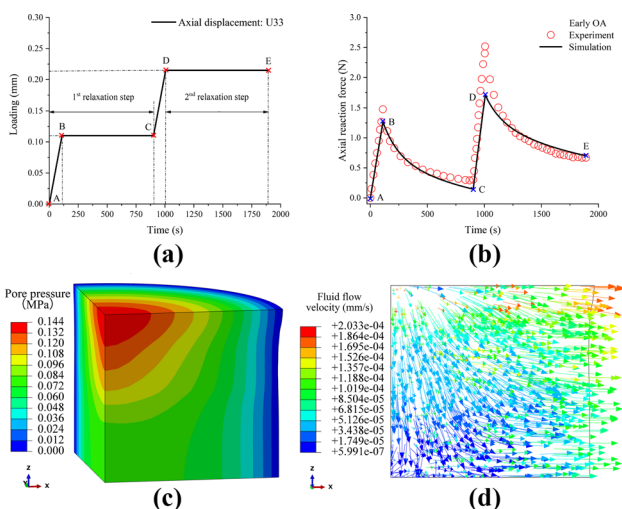


Fig. 8 Simulation results from the unconfined compression test of the early OA sample. **a** Loading protocol used in the simulation of the unconfined compression test (Julkunen et al. 2008). **b** The comparison of stress relaxation data between experimental (Julkunen et al. 2008) and simulation results. Viscoelastic parameters γ_m and τ_m are, respectively, identified as 1.0 and 1050 s to obtain a good agreement with the experimental data. **c, d** show the pore pressure and fluid flow velocity, respectively, at the maximum axial displacement [point D shown in (a, b)]

compressive loading, the highest pore pressure occurs at the centre region of the top surface. The pore pressure gradient shown in Fig. 8c drives the fluid to flow from the relatively higher pressure region to the lower pressure region, and finally, the fluid is extruded through the cylindrical surface where fluid is allowed to freely drain (see Fig. 8d).

5.2 Spherical indentation test

The spherical indentation simulation of the normal AC sample is conducted to validate the proposed damage model by comparing the predicted damage behaviour of AC with a recently published experimental study in (Henao-Murillo et al. 2018). The geometry of the AC sample and the indenter as well as the loading protocol in the simulation are identical to the experimental study (Henao-Murillo et al. 2018). Figure 9a–c shows the comparison of the damage evaluation of the normal AC model between the computational and the experimental results. The damage patterns at four apparent strains (0.3, 0.36, 0.4, 0.53) in the AC are studied. According to the experiment, the apparent strain is defined as the ratio of the compression displacement to the original thickness of the AC layer. In the experimental study (Henao-Murillo et al. 2018), the macroscopic and microscopic damage is related to the clefts of PG matrix and the damage of collagen fibrils, respectively. The damage degree is categorized into five levels. Grade 0 represents that

no significant irregularities or damage is observed in both solid constituents. For the macroscopic damage, the five damage degree are defined as: Grade 1—surface irregularities; Grade 2—surface damage; Grade 3—clefts propagating into the middle zone; Grade 4—clefts propagating into the deep zone; Grade 5—clefts propagating into the calcified zone. For the microscopic damage, the five damage levels are determined by the following criteria: Grade 1—damage in 1/4 of the AC thickness; Grade 2—damage in 1/2 of the AC thickness; Grade 3—damage in 3/4 of the AC thickness; Grade 4—damage in full thickness of AC; Grade 5—damage in full thickness of AC + significant superficial damage. The total damage degree is defined as the summation of macroscopic and microscopic damage degree. The damage degrees of two main solid constituents of AC in the simulations are evaluated according to the scoring system in the experimental study. Figure 9d–g illustrates the damage distributions in the PG matrix of the intact AC model at the four apparent strains. Figure 9h–k demonstrates the damage distributions in the collagen fibril networks of the normal AC model, corresponding to the microscopic internal collagen damage at the four apparent strains in Fig. 9b. It is noted that the CC and SCB layers are not shown in the figures. In the simulations, significant damage regions in the collagen fibril networks enlarge along the deep direction with the increased compression of the spherical indenter. In addition, with the increase in the apparent strain, the damage zone in

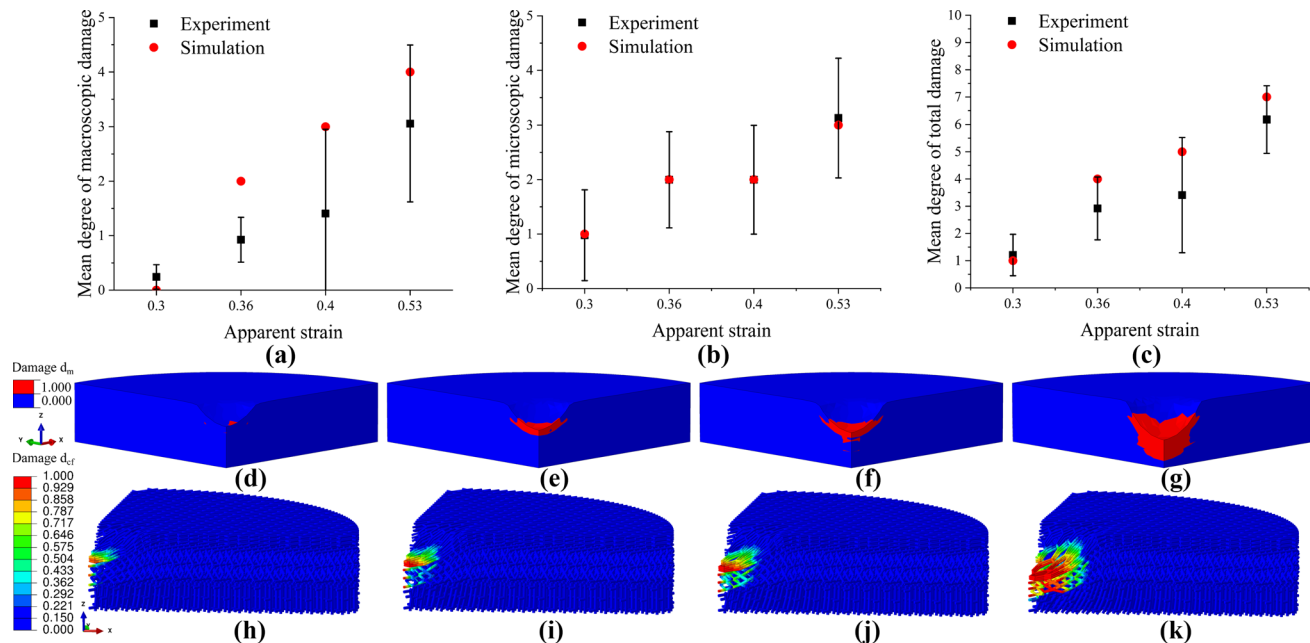


Fig. 9 Comparison between damage degree of AC in simulations and experiments, and illustration of damage propagations with the increase in apparent strains. **a–c** show the mean degree of macroscopic damage, microscopic damage and total damage, respectively, under four apparent strains. **d–g**, respectively, illustrate the damage

distribution in the PG matrix under 0.3, 0.36, 0.4 and 0.53 apparent strain, corresponding to (a). **h–k**, respectively, illustrate the damage distribution in the collagen fibril networks under 0.3, 0.36, 0.4 and 0.53 apparent strain, corresponding to (b)

the PG matrix penetrates from the AC surface to the deep zone and radial zone, which is in line with the macroscopic damage of AC sample in the experiment. Moreover, the total damage degrees at the four compression levels in the simulations agree well with the mean degree of total damage in the experiments. The good agreement between the experimental and computational results indicates that the proposed biphasic visco-hyperelastic damage model parameters used in this study are able to describe the mechanical and damage behaviours of AC.

Figure 10 illustrates the damage distributions in the PG matrix and collagen fibrils of the advanced OA model using different mesh sizes with 22,996 and 47,245 elements at the central zone of AC. The damage is evaluated at the axial compression displacement of 40% of the cartilage thickness. No significant difference in the damage distribution of both PG matrix and collagen fibril networks is observed with the

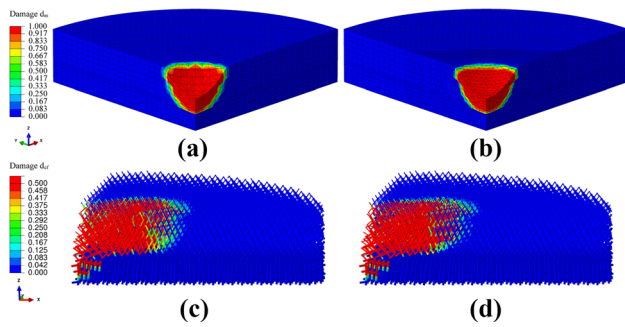


Fig. 10 Mesh sensitivity analysis for damage distributions in PG matrix and collagen fibrils. Damage distributions in the advanced OA samples are extracted at the axial compression displacement of 40% of the cartilage thickness. The model is discretized with two different meshes, consisting of 22,996 (in **a**, **c**) and 47,245 elements (in **b**, **d**), respectively. The same characteristic length l_r of 0.1 mm is used

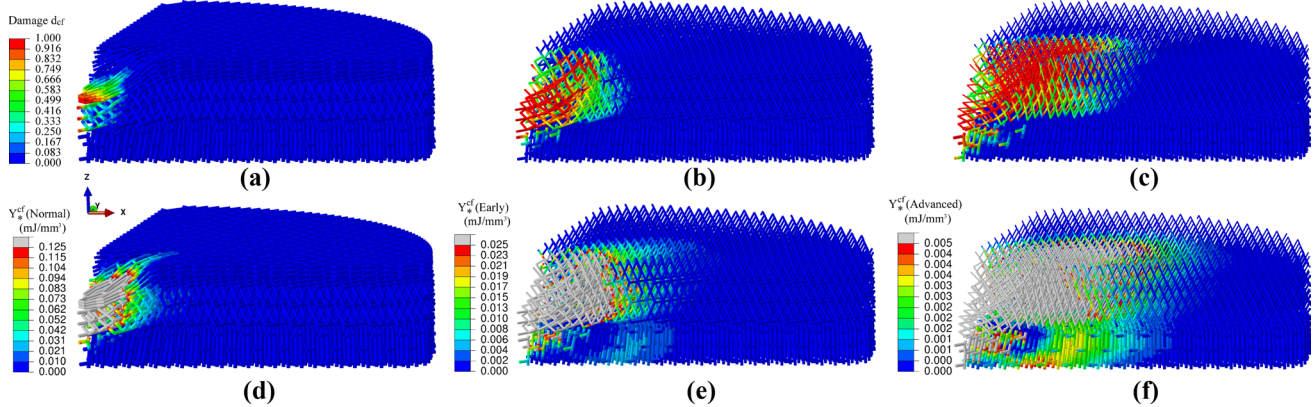


Fig. 11 Fibrils damage in the spherical indentation simulation. **a–c** illustrate the damage in fibrils of normal AC, early OA and advanced OA samples, respectively. **d–f** illustrate the damage driving force in fibrils of normal AC, early OA and advanced OA samples, respec-

change of mesh density. These results show that the mesh dependence has been minimized.

Figure 11a–c illustrates the damage contours of collagen fibrils in the normal AC, early OA and advanced OA specimens in the spherical indentation simulations, respectively. Damage in the normal AC, early OA and advanced OA specimens is evaluated under the compression displacement of about 35%, 42% and 50% of the cartilage thickness, respectively, where the axial compression forces in these models reach the same level. The simulation results show that the OA-induced alterations of the fibrillar structure and orientation, as well as the reduction in tensile stiffness, result in different damage profiles. In the spherical indentation test, these fibril networks in the SZ of the normal AC model are mainly stretched parallel to the AC surface. At this level of compressive load, only the strain energy Y_*^{cf} of the collagen fibril in the central region of the SZ and MZ exceeds Y_0^{cf} (Fig. 11d), so that significant damage in the normal AC mainly concentrates in the central region of SZ and MZ (Fig. 11a). Moreover, this result might suggest that the reinforcement effect of the interconnection-formed collagen fibril networks could effectively prevent the damage from developing further into the deeper layers of AC.

In the early OA model, due to the degrading (softening) of the collagen fibrils and the breakdown of the fibril networks in the SZ, the tension resistance capability of the fibrils in the SZ decreases. In addition, the cross-links are mainly stretched under the indentation loading, while the obliquely distributed primary fibrils in SZ and MZ are firstly realigned. This phenomenon is also observed in the previous literatures (Fathi et al. 2017; Wilson et al. 2005). As a result, the indentation force causes more pronounced strain energy in the cross-links of the MZ beneath the indenter as illustrated in Fig. 11e. This further leads to a larger region of

respectively. The maximums in legends of damage driving forces have been limited to the strain energy density for the damage initiation of corresponding AC samples

damage in the MZ, particularly in the cross-links (Fig. 11b). When OA progresses to the advanced level, due to the breakdown of the cross-links, primary fibrils have a higher tensile strain under the indentation loading. Therefore, the damage occurs in the primary fibrils located in the SZ and MZ of the advanced OA specimen (Fig. 11c). Furthermore, the strain energy density in the fibrils of DZ in the OA specimens exceeds the initial damage resistance Y_0^{cf} , which results in the damage propagation to the DZ layer. In summary, due to the OA-induced deterioration of the strain resistance capability, under the same indentation force, a higher OA grade directly causes a larger damage region in the collagen fibril framework.

The damage distributions in the PG matrix in the normal AC, early OA and moderately advanced OA specimens are illustrated in Fig. 12a–c, respectively. The corresponding strain energy (damage driving force $Y_*^{S_m}$) distributions of the PG matrix are shown in Fig. 12d–f. Damage and strain energy density in PG matrix in Fig. 12 are evaluated at the same compression level as those in collagen fibril networks shown in Fig. 11. At the same compression level, the specimens of a higher OA grade have a larger region of excessive strain energy density (marked by grey colour in Fig. 12d–f) that causes damage in the PG matrix. Compared to the normal AC, the deterioration of the PG matrix, together with the degradation of the fibrils, leads to the development of damage from SZ to DZ of the advanced OA sample. This computational result is in accordance with the experimental observation in (Workman et al. 2017). In this experimental study, a significantly larger amount of structural damage in the fibrils is observed in a more advanced cartilage degeneration under the same impact loading condition. In addition, it was found that impact-induced cracks in AC penetrate from SZ to DZ with the development of AC degeneration.

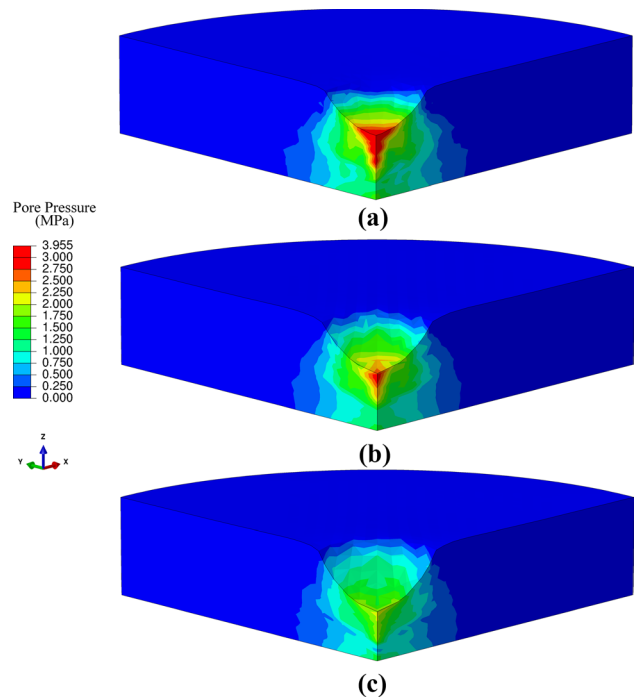


Fig. 13 Pore pressure distributions in the normal AC (a), early OA (b) and advanced OA (c) cartilage samples in the spherical indentation simulations. All graphs show the result at the same compression levels as that in Fig. 11

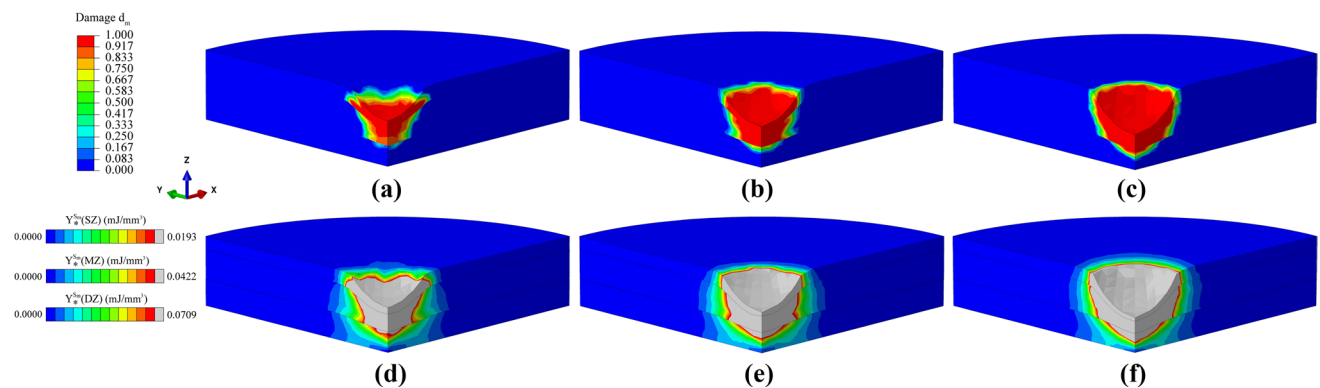


Fig. 12 PG matrix damage in the spherical indentation simulations. a–c illustrate the damage in the matrix of normal AC, early OA and advanced OA samples, respectively. d–f illustrate the damage driving force in the matrix of normal AC, early OA and advanced OA

samples, respectively. The maximums in legends of damage driving forces have been limited to the strain energy density for the damage initiation of corresponding AC samples

and 45% compared to the peak value of the pore pressure in the normal AC.

6 Conclusions

The focus of the current work is to reveal the effect of OA-induced structural and compositional alterations on the damage behaviour of AC. For this purpose, a poro-visco-hyperelastic damage model is developed within the framework of finite strains for describing the nonlinear deformation and the complex damage behaviour of articular cartilages. Furthermore, an integral-type nonlocal averaging algorithm is employed to eliminate the mesh dependence. In addition, 3D microstructural models, involving different morphologies of the collagen fibril networks resulted from the progression of OA, are proposed to simulate and compare the normal AC and OA cartilages. The compositional changes of collagen fibrils, the PG matrix and interstitial fluids with the progression of OA are taken into account in the simulations. Material parameters of the proposed constitutive model are identified by fitting the numerical results with the experimental data from unconfined compression tests. The predicted damage behaviour of the normal AC is quantitatively validated by the experiment data of a spherical indentation test from the literature. In addition, the relation among OA development, fluid pore pressure and the damage evolution is discussed in detail. Based on the above results and discussions, the following conclusions can be drawn:

- The proposed poro-visco-hyperelastic damage model is able to describe the inelastic deformation and damage behaviour of articular cartilages under different loading conditions. The stress relaxation curve obtained from numerical simulations is in good agreement with the experimental result from a previous unconfined compression test. In addition, the predicted damage degree under different compression apparent strains in the PG matrix and collagen fibril networks of the normal AC specimen is in good agreement with the experimental observations.
- The used integral-type nonlocal averaging algorithm can overcome the mesh dependency due to strain localizations in the simulation of articular cartilage. By using this nonlocal algorithm, the damage contours from the simulation with different mesh densities are mesh independent.
- Compared to the normal AC, the deterioration of the PG matrix, together with the degradation of the fibrils induced by OA, leads to a deeper damage development from SZ to DZ in the moderately advanced OA specimen under the same loading conditions.
- The 3D computational simulations involving explicit modelling of the collagen fibril network reveal cross-

links connecting the collagen fibrils play an important role in the deformation and damage resistance of AC. The cross-links enable transverse interconnections in the fibrillar structure and provide a significant stiffening of the microstructure of AC. As a result, it is crucial to maintain the overall load-bearing capability of AC.

The proposed computational methods for studying the relationship between the damage behaviour and the microstructural characteristics of the collagen fibril networks of AC would provide new insights for designing more sophisticated microstructures of novel biomimetic materials with higher damage resistances in cartilage tissue engineering.

Acknowledgements The first author would like to acknowledge the research funding from China Scholarship Council (201606890022).

Compliance with ethical standards

Conflict of interest The authors declare that they have no conflict of interest.

References

- Andrade F, César de Sá J, Andrade Pires F (2011) A ductile damage nonlocal model of integral-type at finite strains: formulation and numerical issues. *Int J Damage Mech* 20(4):515–557
- Andrade F, de Sá JC, Pires FA (2014) Assessment and comparison of non-local integral models for ductile damage. *Int J Damage Mech* 23(2):261–296
- Antons J, Marascio M, Nohava J, Martin R, Applegate L, Bourban P, Pioletti D (2018) Zone-dependent mechanical properties of human articular cartilage obtained by indentation measurements. *J Mater Sci Mater Med* 29(5):57
- Arokoski J, Jurvelin J, Vaatainen U, Helminen H (2000) Normal and pathological adaptations of articular cartilage to joint loading. *Scand J Med Sci Sports* 10(4):186–198
- Bachrach NM, Mow VC, Guilak F (1998) Incompressibility of the solid matrix of articular cartilage under high hydrostatic pressures. *J Biomech* 31(5):445–451
- Balzani D, Ortiz M (2012) Relaxed incremental variational formulation for damage at large strains with application to fiber-reinforced materials and materials with truss-like microstructures. *Int J Numer Meth Eng* 92(6):551–570
- Berger L, Bordas R, Kay D, Tavener S (2017) A stabilized finite element method for finite-strain three-field poroelasticity. *Comput Mech* 60(1):51–68
- Bluhm J (2002) Modelling of saturated thermo-elastic porous solids with different phase temperatures. In: Ehlers W, Bluhm J (eds) *Porous media*. Springer, Berlin, pp 87–118
- Canal Guterl C, Hung CT, Ateshian GA (2010) Electrostatic and non-electrostatic contributions of proteoglycans to the compressive equilibrium modulus of bovine articular cartilage. *J Biomech* 43(7):1343–1350
- Canty EG (2005) Procollagen trafficking, processing and fibrillogenesis. *J Cell Sci* 118(7):1341–1353
- Changoor A, Nelea M, Méthot S, Tran-Khanh N, Chevrier A, Restrepo A, Shive M, Hoemann C, Buschmann M (2011) Structural characteristics of the collagen network in human normal,

- degraded and repair articular cartilages observed in polarized light and scanning electron microscopies. *Osteoarthr Cartil* 19(12):1458–1468
- Choi K, Kuhn J, Ciarelli M, Goldstein S (1990) The elastic moduli of human subchondral, trabecular, and cortical bone tissue and the size-dependency of cortical bone modulus. *J Biomech* 23(11):1103–1113
- Clark JM (1990) The organisation of collagen fibrils in the superficial zones of articular cartilage. *J Anat* 171:117–130
- Clark JM (1991) Variation of collagen fiber alignment in a joint surface: a scanning electron microscope study of the tibial plateau in dog, rabbit, and man. *J Orthop Res* 9(2):246–257
- DiSilvestro M, Suh J (2001) A cross-validation of the biphasic poroviscoelastic model of articular cartilage in unconfined compression, indentation, and confined compression. *J Biomech* 34(4):519–525
- Doyran B, Tong W, Li Q, Jia H, Zhang X, Chen C, Enomoto-Iwamoto M, Lu X, Qin L, Han L (2017) Nanoindentation modulus of murine cartilage: a sensitive indicator of the initiation and progression of post-traumatic osteoarthritis. *Osteoarthr Cartil* 25(1):108–117
- Fathi F, Hatifi Ardakani S, Fatemi Dehaghani P, Mohammadi S (2017) A finite strain integral-type anisotropic damage model for fiber-reinforced materials: application in soft biological tissues. *Comput Methods Appl Mech Eng* 322:262–295
- Ferreira J, Parente M, Jabareen M, Jorge RN (2017) A general framework for the numerical implementation of anisotropic hyperelastic material models including non-local damage. *Biomech Model Mechanobiol* 16(4):1119–1140
- García JJ, Cortés DH (2007) A biphasic viscohyperelastic fibril-reinforced model for articular cartilage: formulation and comparison with experimental data. *J Biomech* 40(8):1737–1744
- Gottardi R, Hansen U, Raiteri R, Loparic M, Düggelin M, Mathys D, Friederich NF, Bruckner P, Stoltz M (2016) Supramolecular organization of collagen fibrils in healthy and osteoarthritic human knee and hip joint cartilage. *PLoS ONE* 11(10):e0163552
- Han L, Grodzinsky AJ, Ortiz C (2011) Nanomechanics of the cartilage extracellular matrix. *Annu Rev Mater Res* 41(1):133–168
- He B, Wu J, Chim S, Xu J, Kirk T (2013) Microstructural analysis of collagen and elastin fibres in the kangaroo articular cartilage reveals a structural divergence depending on its local mechanical environment. *Osteoarthr Cartil* 21(1):237–245
- Henao-Murillo L, Ito K, van Donkelaar CC (2018) Collagen damage location in articular cartilage differs if damage is caused by excessive loading magnitude or rate. *Ann Biomed Eng* 46(4):605–615
- Heuvelmans A, Wilson W, Ito K, van Donkelaar C (2017) The critical size of focal articular cartilage defects is associated with strains in the collagen fibers. *Clin Biomech* 50:40–46
- Hollander AP, Heathfield TF, Webber C, Iwata Y, Bourne R, Rorabeck C, Poole A (1994) Increased damage to type II collagen in osteoarthritic articular cartilage detected by a new immunoassay. *J Clin Investig* 93(4):1722–1732
- Holzapfel GA, Gasser TC (2001) A viscoelastic model for fiber-reinforced composites at finite strains: continuum basis, computational aspects and applications. *Comput Methods Appl Mech Eng* 190(34):4379–4403
- Hosseini S, Wilson W, Ito K, Van Donkelaar C (2014) A numerical model to study mechanically induced initiation and progression of damage in articular cartilage. *Osteoarthr Cartil* 22(1):95–103
- Hui Mingalone CK, Liu Z, Hollander JM, Garvey KD, Gibson AL, Banks RE, Zhang M, McAlindon TE, Nielsen HC, Georgakoudi I, Zeng L (2018) Bioluminescence and second harmonic generation imaging reveal dynamic changes in the inflammatory and collagen landscape in early osteoarthritis. *Lab Investig* 98(5):656–669
- Hwang W, Li B, Jin L, Ngo K, Schachar N, Hughes G (1992) Collagen fibril structure of normal, aging, and osteoarthritic cartilage. *J Pathol* 167(4):425–433
- Inamdar SR, Knight DP, Terrill NJ, Karunaratne A, Cacho-Nerin F, Knight MM, Gupta HS (2017) The secret life of collagen: temporal changes in nanoscale fibrillar pre-strain and molecular organization during physiological loading of cartilage. *ACS Nano* 11(10):9728–9737
- Jirásek M (2007) Nonlocal damage mechanics. *Rev Eur Génie Civ* 11(7–8):993–1021
- Julkunen P, Wilson W, Jurvelin JS, Rieppo J, Qu C, Lammi MJ, Korhonen RK (2008) Stressrelaxation of human patellar articular cartilage in unconfined compression: prediction of mechanical response by tissue composition and structure. *J Biomech* 41(9):1978–1986
- Kaliske M, Rothert H (1997) Formulation and implementation of three-dimensional viscoelasticity at small and finite strains. *Comput Mech* 19(3):228–239
- Klika V, Gaffney EA, Chen Y, Brown CP (2016) An overview of multiphase cartilage mechanical modelling and its role in understanding function and pathology. *J Mech Behav Biomed Mater* 62:139–157
- Korhonen RK, Laasanen MS, Töyräs J, Lappalainen R, Helminen HJ, Jurvelin JS (2003) Fibril reinforced poroelastic model predicts specifically mechanical behavior of normal, proteoglycan depleted and collagen degraded articular cartilage. *J Biomech* 36(9):1373–1379
- Lane L, Bullough P (1980) Age-related changes in the thickness of the calcified zone and the number of tidemarks in adult human articular cartilage. *J Bone Joint Surg Br* 62(3):372–375
- Lewis JL, Johnson SL (2001) Collagen architecture and failure processes in bovine patellar cartilage. *J Anat* 199(4):483–492
- Liukkonen MK, Mononen ME, Klets O, Arokoski JP, Saarakkala S, Korhonen RK (2017) Simulation of subject-specific progression of knee osteoarthritis and comparison to experimental follow-up data: data from the osteoarthritis initiative. *Sci Rep* 7(1):1–14
- Ma S, Yuan H (2015) Computational investigation of multi-axial damage modeling for porous sintered metals with experimental verification. *Eng Fract Mech* 149:89–110
- Ma S, Scheider I, Bargmann S (2016a) Anisotropic constitutive model incorporating multiple damage mechanisms for multiscale simulation of dental enamel. *J Mech Behav Biomed Mater* 62:515–533
- Ma S, Scheider I, Bargmann S (2016b) Continuum damage modeling and simulation of hierarchical dental enamel. *Modell Simul Mater Sci Eng* 24(4):45014
- Ma S, Zhou B, Markert B (2018) Numerical simulation of the tissue differentiation and corrosion process of biodegradable magnesium implants during bone fracture healing. *ZAMM J Appl Math Mech/Z Angew Math Mech* 98(12):2223–2238
- Mäkelä J, Cooper B, Korhonen R, Grinstaff M, Snyder B (2018) Functional effects of an interpenetrating polymer network on articular cartilage mechanical properties. *Osteoarthr Cartil* 26(3):414–421
- Mansfield J, Bell J, Winlove C (2015) The micromechanics of the superficial zone of articular cartilage. *Osteoarthr Cartil* 23(10):1806–1816
- Men Y, Jiang Y, Chen L, Zhang C, Ye J (2017) On mechanical mechanism of damage evolution in articular cartilage. *Mater Sci Eng C* 78:79–87
- Mente P, Lewis J (1994) Elastic modulus of calcified cartilage is an order of magnitude less than that of subchondral bone. *J Orthop Res* 12(5):637–647
- Mononen M, Julkunen P, Töyräs J, Jurvelin J, Kiviranta I, Korhonen R (2011) Alterations in structure and properties of collagen network of osteoarthritic and repaired cartilage modify knee joint stresses. *Biomech Model Mechanobiol* 10(3):357–369
- Mononen ME, Tanska P, Isaksson H, Korhonen RK (2016) A novel method to simulate the progression of collagen degeneration of cartilage in the knee: data from the osteoarthritis initiative. *Sci Rep* 6(1):21415

- Mow VC, Holmes MH, Michael Lai W (1984) Fluid transport and mechanical properties of articular cartilage: a review. *J Biomech* 17(5):377–394
- Mow VC, Ratcliffe A, Robin Poole A (1992) Cartilage and diarthrodial joints as paradigms for hierarchical materials and structures. *Biomaterials* 13(2):67–97
- Natarajan V, Madhan B, Tiku ML (2015) Intra-articular injections of polyphenols protect articular cartilage from inflammation-induced degradation: suggesting a potential role in cartilage therapeutics. *PLoS ONE* 10(6):e0127165
- Nickien M, Thambyah A, Broom N (2013) How changes in fibril-level organization correlate with the macrolvel behavior of articular cartilage. *Wiley Interdiscip Rev Syst Biol Med* 5(4):495–509
- Párraga Quiroga J, Wilson W, Ito K, van Donkelaar C (2017) The effect of loading rate on the development of early damage in articular cartilage. *Biomech Model Mechanobiol* 16(1):263–273
- Peña E (2011a) A rate dependent directional damage model for fibred materials: application to soft biological tissues. *Comput Mech* 48(4):407–420
- Peña E (2011b) Prediction of the softening and damage effects with permanent set in fibrous biological materials. *J Mech Phys Solids* 59(9):1808–1822
- Pierce DM, Ricken T, Holzapfel GA (2013) A hyperelastic biphasic fibre-reinforced model of articular cartilage considering distributed collagen fibre orientations: continuum basis, computational aspects and applications. *Comput Methods Biomed Eng* 16(12):1344–1361
- Pierce DM, Unterberger MJ, Trobin W, Ricken T, Holzapfel GA (2016) A microstructurally based continuum model of cartilage viscoelasticity and permeability incorporating measured statistical fiber orientations. *Biomech Model Mechanobiol* 15(1):229–244
- Richard F, Villars M, Thibaud S (2013) Viscoelastic modeling and quantitative experimental characterization of normal and osteoarthritic human articular cartilage using indentation. *J Mech Behav Biomed Mater* 24:41–52
- Ricken T, Dahmen U, Dirsch O (2010) A biphasic model for sinusoidal liver perfusion remodeling after outflow obstruction. *Biomech Model Mechanobiol* 9(4):435–450
- Saarakkala S, Julkunen P, Kiviranta P, Mäkitalo J, Jurvelin J, Korhonen R (2010) Depth-wise progression of osteoarthritis in human articular cartilage: investigation of composition, structure and biomechanics. *Osteoarthr Cartil* 18(1):73–81
- Schinagl RM, Gurskis D, Chen AC, Sah RL (1997) Depth-dependent confined compression modulus of full-thickness bovine articular cartilage. *J Orthop Res* 15(4):499–506
- Sophia Fox AJ, Bedi A, Rodeo SA (2009) The basic science of articular cartilage: structure, composition, and function. *Sports Health* 1(6):461–468
- Stender ME, Regueiro RA, Klisch SM, Ferguson VL (2015) An equilibrium constitutive model of anisotropic cartilage damage to elucidate mechanisms of damage initiation and progression. *J Biomech Eng* 137(8):081010
- Stender ME, Carpenter RD, Regueiro RA, Ferguson VL (2016) An evolutionary model of osteoarthritis including articular cartilage damage, and bone remodeling in a computational study. *J Biomech* 49(14):3502–3508
- Thambyah A, Broom N (2007) On how degeneration influences load-bearing in the cartilagebone system: a microstructural and micro-mechanical study. *Osteoarthr Cartil* 15(12):1410–1423
- Torzilli P, Grigiene R, Borrelli J, Helfet D (1999) Effect of impact load on articular cartilage: cell metabolism and viability, and matrix water content. *J Biomech Eng* 121(5):433–441
- Van der Voet A (1997) A comparison of finite element codes for the solution of biphasic poroelastic problems. *Proc Inst Mech Eng H* 211(2):209
- Vanden Berg-Foels W, Scipioni L, Huynh C, Wen X (2012) Helium ion microscopy for high-resolution visualization of the articular cartilage collagen network. *J Microsc* 246(2):168–176
- Waffenschmidt T, Polindara C, Menzel A, Blanco S (2014) A gradient-enhanced large-deformation continuum damage model for fibre-reinforced materials. *Comput Methods Appl Mech Eng* 268:801–842
- Wen C, Wu C, Tang B, Wang T, Yan C, Lu W, Pan H, Hu Y, Chiu K (2012) Collagen fibril stiffening in osteoarthritic cartilage of human beings revealed by atomic force microscopy. *Osteoarthr Cartil* 20(8):916–922
- Wilson W, van Donkelaar C, van Rietbergen R, Huiskes R (2005) The role of computational models in the search for the mechanical behavior and damage mechanisms of articular cartilage. *Med Eng Phys* 27(10):810–826
- Wilson W, Driessens N, van Donkelaar C, Ito K (2006a) Prediction of collagen orientation in articular cartilage by a collagen remodeling algorithm. *Osteoarthr Cartil* 14(11):1196–1202
- Wilson W, Huyghe J, van Donkelaar C (2006b) A composition-based cartilage model for the assessment of compositional changes during cartilage damage and adaptation. *Osteoarthr Cartil* 14(6):554–560
- Wilson W, Huyghe J, van Donkelaar C (2007) Depth-dependent compressive equilibrium properties of articular cartilage explained by its composition. *Biomech Model Mechanobiol* 6(1–2):43–53
- Wilusz R, Zauscher S, Guilak F (2013) Micromechanical mapping of early osteoarthritic changes in the pericellular matrix of human articular cartilage. *Osteoarthr Cartil* 21(12):1895–1903
- Workman J, Thambyah A, Broom N (2017) The influence of early degenerative changes on the vulnerability of articular cartilage to impact-induced injury. *Clin Biomech* 43:40–49

Publisher's Note Springer Nature remains neutral with regard to jurisdictional claims in published maps and institutional affiliations.